QUANTIFYING THE EFFECTS OF LATERAL ADVECTION ON SHEAR MARGIN THERMAL STRUCTURE AND MELTWATER PRODUCTION

by

PIERCE ANDREW HUNTER

A THESIS

Presented to the Department of Earth Sciences
and the Graduate School of the University of Oregon
in partial fulfillment of the requirements
for the degree of
Master of Science

September 2020

THESIS APPROVAL PAGE

Student: Pierce Andrew Hunter

Title: Quantifying the Effects of Lateral Advection on Shear Margin Thermal Structure and Meltwater Production

This thesis has been accepted and approved in partial fulfillment of the requirements for the Master of Science degree in the Department of Earth Sciences by:

Alan Rempel	Chairperson
Dave Sutherland	Member
Brittany Erickson	Member

and

Kate Mondloch	Interim Vice Provost and Dean of the Graduate School

Original approval signatures are on file with the University of Oregon Graduate School.

Degree awarded September 2020

THESIS ABSTRACT

Pierce Andrew Hunter

Master of Science

Department of Earth Sciences

September 2020

Title: Quantifying the Effects of Lateral Advection on Shear Margin Thermal Structure and Meltwater Production

Ice stream discharge is controlled through a balance between gravity, basal friction, and side drag. The interplay between advective cooling and shear heating along bounding ice ridges controls the temperature-dependent viscosity structure that determines how side drag drives marginal strain rates. Ultimately, the development of temperate ice can cause dramatic softening and internal melting, with the potential to alter basal friction. Here, we present a two-dimensional (three velocity component), steady-state model focussed on an idealized cross section and identify key scalings for the emergence of temperate conditions. We validate our treatment against the behavior of the Bindschadler Ice Stream and explore potential future behavior uinge CMIP5 forecasts for changes in surface forcing. Steady states under the conditions that are expected by 2300 would increase centerline ice stream velocity by up to 200% and shear melting by up to 750%, while nearly tripling the total meltwater supply to the bed.

CURRICULUM VITAE

NAME OF AUTHOR: Pierce Andrew Hunter

GRADUATE AND UNDERGRADUATE SCHOOLS ATTENDED:

University of Oregon, Eugene
University of California, Los Angeles
Diablo Valley College

DEGREES AWARDED:

Master of Science, 2020, University of Oregon
Bachelor of Science, 2018, University of Oregon

AREAS OF SPECIAL INTEREST:

Applied Mathematics
Computational Mathematics
Geophysics
Computer Science

ACKNOWLEDGMENTS

I wish to express my sincere appreciation to Dr. Alan Rempel (University of Oregon), and Dr. Colin Meyer (Dartmouth College) for their assistance in the preparation of this manuscript, and the study conducted therein. I also express my deepest gratitude to Dave Sutherland and Brittany Erickson for their careful review of this document in preparation for submission, as well as Kiya Riverman and Joshua Crozier for assisting with specific components pertaining to my research.

TABLE OF CONTENTS

LIST OF FIGURES

LIST OF TABLES

I INTRODUCTION

Outlet glaciers are responsible for most of the ice discharge from Antarctica to the ocean. The Antarctic Ice Sheet is in extreme cold so surface melt is minimal and meltwater supplied to the glacier bed is almost entirely derived from viscous dissipation within the ice and friction along the bed. Excess meltwater at the bed can reduce friction within tills, promoting faster downstream flow and ice stream widening [Jacobson and Raymond, 1998; Haseloff et al., 2018]. Increased ice stream flux is often supplied by lateral inflow from bordering, comparatively stagnant ice ridges; the transition between these fast and slow flowing regions is an area of immense shear called a shear margin. Viscous dissipation increases temperatures and softens ice in these shear margins. However, lateral advection of cold ice from the ridge to the stream has potential to reduce temperatures within the margin, resulting in higher ice viscosities that can reduce strain rates and lower meltwater generation rates [Haseloff et al., 2015, 2018]. Quantifying the dynamic relationship between lateral advection and shear heating under realistic conditions is paramount to understanding the current environmental status of Antarctica and its susceptibility to climate change.

As the ice within a shear margin warms, it softens due to the temperature-dependence of the ice rheology. The softer ice is less resistant to flow, allowing increased downstream flux and leading to higher shear rates throughout the margin, resulting in a thermoviscous feedback. Ultimately, the shear within the margin may cause sufficient heating to produce temperate ice—ice at the melting point. Any

additional shear heating within the temperate zone contributes directly to internal melting. However, cold ice influx from a bounding ice ridge—lateral advection—can cool the margin, stiffen the ice, and reduce shear heating, thus leading to a smaller temperate zone. The formation of temperate ice in a shear margin is sensitive to surface temperature and snow accumulation [Meyer and Minchew, 2018]. Increased surface temperatures suppress conductive transport away from the shear margin, leading to larger temperate zones, whereas greater snow accumulation increases vertical advective cooling, leading to a reduction in temperate ice. Lateral advection, proportional to snow accumulation in supplying catchments, can cause significant cooling that must also be considered when modeling shear margin behavior.

Early studies of shear margin dynamics incorporated temperature-dependent ice rheology and focused on how temperature influences the location of shear margins [Jacobson and Raymond, 1998; Suckale et al., 2014]. To better pinpoint thermal effects, these models utilized a simplified physical description of lateral advection. More recent studies have estimated rates of ice stream widening in relation to lateral advection and sub-temperate slip [Schoof, 2012; Haseloff et al., 2015, 2018], however, to better highlight stress relations, the temperature-dependent ice rheology was neglected. Perol and Rice [2015] developed a one-dimensional model investigating the relation between the lateral components of stress and strain, ultimately concluding Antarctic shear margins are likely to contain a substantial fraction of temperate ice due to localized high strain rates. Meyer and Minchew [2018] also conducted a one-

dimensional study in which physical balances gauged by dimensionless parameters informed a mapping of temperate zone thicknesses across the continent of Antarctica, further supporting the expectation that substantial temperate ice volumes are likely in a large number of Antarctic shear margins. Haseloff et al. [2019] developed a more sophisticated one-dimensional treatment that incorporates the effects of melt water content on ice rheology and shear margin evolution using an analytical approximation for lateral advection.

Here, we develop a two-dimensional, steady-state model for shear margin thermomechanics that envelops both temperature dependent ice rheology and lateral advection. We solve for downstream velocity through the momentum balance equation, in which viscous forcing balances gravitational forcing, and solve for temperature through the energy balance equation, where thermal diffusion is balanced by shear heating paired with lateral and vertical advection. We extract key parameter ratios by nondimensionalizing our equations, and use those relationships to guide parameter choices that are representative of Antarctic conditions, which allows us to quantify how temperate ice volume and melt rates vary across a broad range of realistic conditions. We then model a natural system by executing a case study of Bindschadler Ice Stream—a ridge-controlled glacier with two distinct flow regimes—and find our model conforms well to surface data and previous studies [e.g. Meyer et al., 2018]. We look for temperate ice and meltwater distribution in Bindschadler under current conditions and also when applying CMIP5 predicted climate change models, RCP

4.5 and RCP 8.5, forecast to the years 2100 and 2300. At steady state under these warmer climates, we predict that a Bindschadler-like ice stream would experience up to a 700% increase in shear meltwater generation, potentially causing basal shear resistance to evolve. The dramatic changes under climate forcing representative of conditions forecast in the coming centuries impresses the need for a detailed model able to simulate a wide range of parameter choices.

II THEORY

Model Physics

We develop a two-dimensional (three velocity component), steady-state model for ice stream flow u in the x-direction. We assume symmetry about the stream center ($y = 0$), with margin locations $y = \pm W_m$ and outer ridge boundaries $y = \pm W$—for a total stream width $2W_m$, and total domain width $2W$. We hold thickness H constant, with bed location $z = 0$, applying a surface slope α to the entire domain. The model geometry is depicted in Fig. 1, and we choose to plot in $-y$, meaning the ridge is on the left, and stream on the right. Conservation of mass throughout the domain is

$$\frac{\partial u}{\partial x} + \frac{\partial v}{\partial y} + \frac{\partial w}{\partial z} = 0, \tag{1}$$

which describes incompressible flow with lateral velocity component v and vertical velocity component w. The downstream velocity u is determined by balancing gravitational forcing ($\rho g \sin \alpha$) by viscous flow through

$$\frac{\partial}{\partial y}\left(\eta \frac{\partial u}{\partial y}\right) + \frac{\partial}{\partial z}\left(\eta \frac{\partial u}{\partial z}\right) = -\rho g \sin \alpha, \tag{2}$$

where η is the temperature- and strain-rate-dependent ice viscosity. We allow free slip at the surface, no slip on the ridge boundaries (along $z = 0$ for $|y| > W_m$ and along $|y| = W$ for all z) and apply a fixed basal frictional stress τ_b under the stream

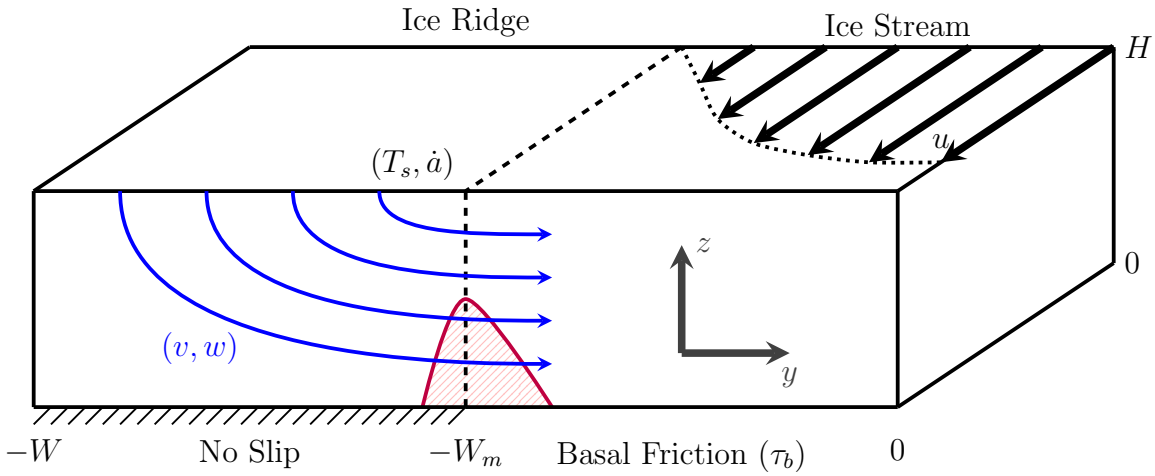

Figure 1: Model geometry sketch. An ice stream of width $2W_m$ and thickness H is bordered on either side by an ice ridge. We apply a no-slip boundary under the ridge and basal friction under the stream. Lateral and vertical advection (v and w) are specified throughout the domain. We apply a constant surface temperature T_s and average annual accumulation rate $\dot{a}$. The red-hatched region is a representative temperate ice zone. We assume symmetry about the stream center, so only the left half of the domain is modeled to determine the downstream velocity (u) and temperature (T) fields.

Parameter	**Description**	**Value**
A_*	ice softness control parameter	$3.5 \times 10^{-25}\,\mathrm{Pa^{-n}\,s^{-1}}$
c_1	heat capacity constant	$152.5\ \mathrm{J\,kg^{-1}\,K^{-1}}$
c_2	heat capacity constant	$7.122\ \mathrm{J\,kg^{-1}\,K^{-2}}$
g	gravitational acceleration	$9.81\ \mathrm{m\,s^{-2}}$
k_1	thermal conductivity pre-factor	$9.828\ \mathrm{W\,m^{-1}\,K^{-1}}$
k_2	thermal conductivity exponential factor	$-5.7 \times 10^{-3}\,\mathrm{K^{-1}}$
n	Glen's flow law parameter	3
Q_h	activiation energy ($T > T_*$)	$115\,\mathrm{kJ\,mol^{-1}\,K^{-1}}$
Q_l	activiation energy ($T < T_*$)	$60\,\mathrm{kJ\,mol^{-1}\,K^{-1}}$
R	ideal gas constant	$8.314\,\mathrm{J\,K^{-1}\,mol^{-1}}$
ρ	density of ice	$917\ \mathrm{kg\,m^{-3}}$
T_m	ice melting temperature	273.15 K
T_*	ice softness control temperature	263.15 K

Table 1: Physical constants used in all model runs.

(with $z = 0$ and $|y| < W_m$). We also enforce symmetry at the stream center. With these considerations, the boundary conditions on downstream velocity are written as

$$\frac{\partial u}{\partial z} = 0 \text{ at } z = H; \qquad \frac{\partial u}{\partial y} = 0 \text{ at } y = 0; \qquad u = 0 \text{ at } |y| = W; \tag{3a-c}$$

$$u = 0 \text{ at } W_m \leq |y| \leq W,\ z = 0; \qquad \eta \frac{\partial u}{\partial z} = -\tau_b \text{ at } 0 \leq |y| \leq W_m,\ z = 0. \tag{3d-e}$$

Viscosity is related to temperature and effective strain-rate $\dot{\epsilon}_E$ according to Glen's law with flow exponent n, so that

$$\eta = \frac{1}{2} A^{-1/n} \dot{\epsilon}_E^{(1-n)/n}, \tag{4}$$

with A as the Arrhenius relation [Cuffey and Paterson, 2010]

$$A = A_* \exp\left(-\frac{Q}{R}\left[\frac{1}{T} - \frac{1}{T_*}\right]\right); \qquad Q = \begin{cases} Q_l & T < T_* \\ \\ Q_h & T > T_*. \end{cases} \tag{5}$$

The values of all constants are listed in Table 1. We calculate the effective strain rate as

$$\dot{\epsilon}_E = \frac{1}{2}\left[\left(\frac{\partial u}{\partial y}\right)^2 + \left(\frac{\partial u}{\partial z}\right)^2 + \left(\frac{\partial v}{\partial z} + \frac{\partial w}{\partial y}\right)^2 + 2\left(\frac{\partial v}{\partial y}\right)^2 + 2\left(\frac{\partial w}{\partial z}\right)^2\right]^{1/2} \tag{6}$$

where we use the analytical approximations for vertical and lateral advection that are described in Sec. 2.2 [Haseloff et al., 2019].

Temperature is determined by balancing conduction with advection and shear

heating through

$$\frac{\partial}{\partial y}\left(k\frac{\partial T}{\partial y}\right)+\frac{\partial}{\partial z}\left(k\frac{\partial T}{\partial z}\right)=\rho c\left(v\frac{\partial T}{\partial y}+w\frac{\partial T}{\partial z}\right)-\psi, \tag{7}$$

where we include a linear temperature dependence for heat capacity $c = c_1 + c_2 T$ and an exponential temperature dependence for the thermal conductivity $k = k_1 \exp(-k_2 T)$ [Cuffey and Paterson, 2010]. The shear heating ψ is related to temperature and strain-rate by

$$\psi = 2A^{-1/n}\dot{\epsilon}_E^{(n+1)/n}. \tag{8}$$

For boundary conditions, we apply a constant surface temperature T_s and constrain the bed to the melting temperature T_m, while assuming the stream center and outer ridge boundaries are symmetric, in summary

$$T = T_s \text{ at } z = H, \qquad T = T_m \text{ at } z = 0, \tag{9a-b}$$

$$\frac{\partial T}{\partial y} = 0 \text{ at } |y| = W \text{ and } y = 0. \tag{9c-d}$$

To adapt this model description of ice stream behavior to different settings, alongside the key physical constants, we must assign the geometric parameters α, H, W_m, and W; the basal shear resistance τ_b; the surface temperature T_s; and accumulation rate $\dot{a}$, which enters through the description of advection that we outline next.

Advection

We adapt the analytical approximation for advection presented by Haseloff et al. [2019] to be consistent with a flat surface that simplifies our numerical implementation, and parameterize lateral and vertical advection throughout. This analysis proceeds from a mass balance argument, which requires that accumulation rate $\dot{a}$ be balanced by the depth averaged lateral and vertical flow, so that eq (1) integrates to

$$\frac{\partial \bar{u}}{\partial x} + \frac{\partial \bar{v}}{\partial y} = \frac{\dot{a}}{H}. \tag{10}$$

In the ridge, where downstream velocities are minimal, we expect lateral advection to dominate; and in the stream, where downstream velocity far outweighs lateral velocity we expect downstream flow to dominate. Using the shallow ice approximation, the lateral advection is approximately

$$v = \frac{\dot{a}}{H} \begin{cases} y - \dfrac{n+2}{n+1}\dfrac{W}{W_m} y \left[1 - \dfrac{1}{n+2}\left(\dfrac{y}{W_m}\right)^{n+1}\right] & |y| \leq W_m \\ -\dfrac{n+2}{n+1}\dfrac{y}{|y|}\left(W - |y|\right)\left[1 - \left(1 - \dfrac{z}{H}\right)^{n+1}\right] & W_m \leq |y| \leq W, \end{cases} \tag{11}$$

which implies vertical advection of

$$w = \dot{a} \begin{cases} -\dfrac{z}{H} & |y| \leq W_m \\ -\dfrac{n+2}{n+1}\dfrac{z}{H} + \dfrac{1}{n+1}\left[1 - \left(1 - \dfrac{z}{H}\right)^{n+2}\right] & W_m \leq |y| \leq W. \end{cases} \tag{12}$$

The supplemental materials contain an expanded derivation of (11) and (12). An example of the advection profile in an idealized stream is shown in Fig. 2. Lateral advection is typically about an order of magnitude faster than vertical advection. Note, as well, that both of these components decrease dramatically towards the bed where we expect temperate conditions to first develop.

Nondimensionalization

We nondimensionalize the governing equations to gauge the relative importance of each physical effects. We define two aspect ratios (δ_y and δ_z) and three key nondimensional parameters ($\mathtt{Ga}, \mathtt{Pe}$, and $\mathtt{Br}$). δ_y is defined as the ratio between domain half-width (W) and ice stream half-width (W_m) and δ_z is the ratio between thickness (H) and ice stream half-width. The Galilei number ($\mathtt{Ga}$) is the ratio of gravitational forcing to viscous forcing, the Péclet number ($\mathtt{Pe}$) the ratio of advection to conduction, and the Brinkman number ($\mathtt{Br}$) the ratio of shear heating to conduction. The full expressions for these dimensionless ratios are provided in Table 2, with the stream center velocity u_c and $(T_m - T_s)$ chosen as characteristic scales. Nondimensional equations (2) and (7) are

$$\delta_z^2 \frac{\partial}{\partial \mathcal{Y}} \left(\mu \frac{\partial \mathcal{U}}{\partial \mathcal{Y}} \right) + \frac{\partial}{\partial \mathcal{Z}} \left(\mu \frac{\partial \mathcal{U}}{\partial \mathcal{Z}} \right) = -\mathtt{Ga}, \tag{13}$$

$$\delta_z^2 \frac{\partial}{\partial \mathcal{Y}} \left(\mathcal{K} \frac{\partial \mathcal{T}}{\partial \mathcal{Y}} \right) + \frac{\partial}{\partial \mathcal{Z}} \left(\mathcal{K} \frac{\partial \mathcal{T}}{\partial \mathcal{Z}} \right) = \mathtt{Pe}\, \mathcal{C} \left(\mathcal{V} \frac{\partial \mathcal{T}}{\partial \mathcal{Y}} + \mathcal{W} \frac{\partial \mathcal{T}}{\partial \mathcal{Z}} \right) - \mathtt{Br}\, \Psi, \tag{14}$$

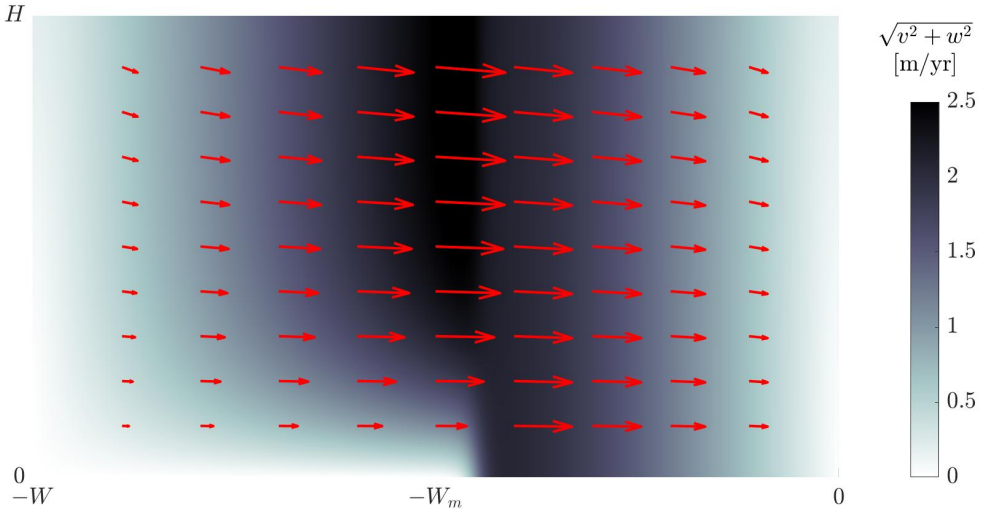

Figure 2: The combined lateral and vertical advection profile for an idealized stream assuming 20 cm/yr accumulation. No slip is assumed under the ridge ($W_m \leq |y| \leq W$), and fixed basal friction is applied under the stream ($0 \leq |y| \leq W_m$). Lateral advection dominates through the majority of the cross-section.

nondimensional parameter	**description**	**equation**
δ_y	$\dfrac{\text{domain half-width}}{\text{ice stream half-width}}$	$\dfrac{W}{W_m}$
δ_z	$\dfrac{\text{ice stream thickness}}{\text{ice stream half-width}}$	$\dfrac{H}{W_m}$
`Ga`	$\dfrac{\text{gravitational forcing}}{\text{viscous forcing}}$	$\rho g \sin\alpha \left[\dfrac{A_* H^{n+1}}{u_c}\right]^{1/n}$
`Pe`	$\dfrac{\text{advective heat transport}}{\text{thermal conduction}}$	$\dfrac{\rho \dot{a} H \left(c_1 + c_2 T_m\right)}{k_1 \exp\left(k_2 T_m\right)}$
`Br`	$\dfrac{\text{shear heating}}{\text{thermal conduction}}$	$\dfrac{A_*^{-1/n} u_c^{(n+1)/n} H^{(n-1)/n}}{k_1 \exp\left(k_2 T_m\right)\left(T_m - T_s\right)}$

Table 2: Key nondimensional parameters described physically and in equation form

where script denotes a dimensionless variable. Here μ and Ψ are the nondimensional forms of viscosity and shear heating respectively. The advection equations from (11) and (12) become

$$\mathcal{V} = \begin{cases} \mathcal{Y} - \dfrac{n+2}{n+1}\delta_y \mathcal{Y}\left[1 - \dfrac{1}{n+2}\mathcal{Y}^{n+1}\right] & |\mathcal{Y}| \leq 1 \\ -\dfrac{n+2}{n+1}\dfrac{\mathcal{Y}}{|\mathcal{Y}|}\left(\delta_y - |\mathcal{Y}|\right)\left[1 - (1-\mathcal{Z})^{n+1}\right] & 1 \leq |\mathcal{Y}| \leq \delta_y; \end{cases} \tag{15}$$

$$\mathcal{W} = \begin{cases} -\mathcal{Z} & |\mathcal{Y}| \leq 1 \\ -\dfrac{n+2}{n+1}\mathcal{Z} + \dfrac{1}{n+1}\left[1 - (1-\mathcal{Z})^{n+2}\right] & 1 \leq |\mathcal{Y}| \leq \delta_y, \end{cases} \tag{16}$$

with $0 \leq \mathcal{Z} \leq 1$. We enforce continuity in the advection equations via a twice-differentiable step function active over the outer 20% of the stream, and solve the coupled system of equations (13-16) to steady-state in COMSOL Multiphysics using finite elements on a meshgrid with increased resolution near the slip/no-slip transition point along the bed ($|\mathcal{Y}| = 1$). A resolution analysis can be found in the supplemental materials.

III DATA & RESULTS

Modeling an Idealized Stream

To explore the range of shear margin behavior expected under a broad spectrum of realistic forcing, we analyze our model predictions and the associated combinations of Brinkman, Péclet and Galilei numbers that emerge based on present geometrical and surface conditions in Antarctica. We utilized measured data bundled in the QGIS package Quantarctica3 provided by the Norwegian Polar Institute [Matsuoka et al., 2018]. This package includes RACMO 2.3 [Van Wessem et al., 2014] which provides surface temperature (T_s) and annual surface mass balance ($\dot{a}$); BEDMAP2 [Fretwell et al., 2013] providing ice thickness (H); and MEaSUREs which provides grounding lines and surface flow speed (u) [Rignot et al., 2011; Mouginot et al., 2012]. We then cast these data to a regular, polarstereo grid and eliminate locations where one or more of the data sets are undefined—an indication that the location is not covered in ice. The compiled data are presented in Fig. 3, with high resolution images found in the supplemental materials.

For simplicity we exclude the Antarctic Peninsula from our study, limiting the scope to only the main continent, allowing us to assume the absence of surface melt. This also provides a range of surface temperatures and accumulation rates that are most representative of the ice streams with which we are interested. We take data from cross-sections of eleven key Antarctic ice streams (detail in Table 3, and num-

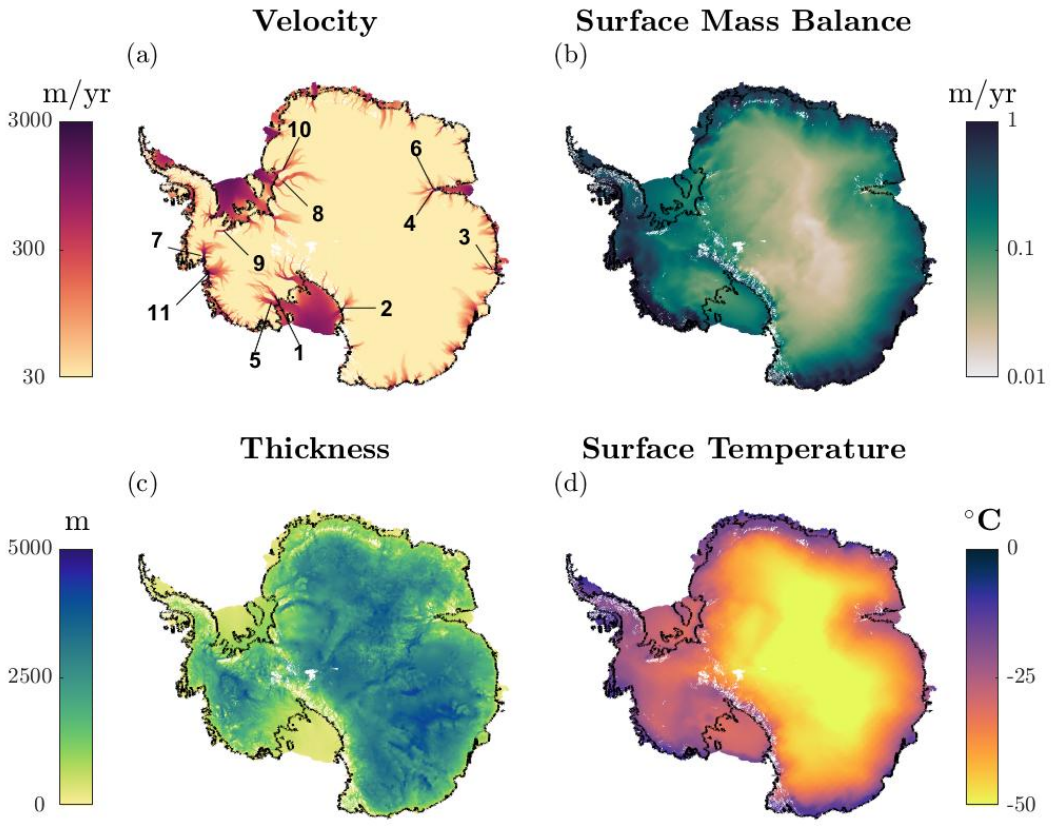

Figure 3: Data taken from surface measurments: (a) velocity data from MeASUREs (log scale) [Rignot et al., 2011; Mouginot et al., 2012], (b) surface mass balance from RACMO 2.3 (log scale) [Van Wessem et al., 2014], (c) thickness data from BEDMAP2 [Fretwell et al., 2013], (d) surface temperature data from RACMO 2.3. The glaciers labeled in (a) correspond to the glacier list in Table 3.

Ice	Stream	H [m]	W_m [km]	$\dot{a}$ [cm/yr]	T_s [°C]	$\sin\alpha$	u_c [m/yr]	Ga	Pe	Br
1	Bindschadler	900	24	7	-29	0.001	700	0.020	1.9	140
2	Byrd	1300	11	25	-31	0.008	800	0.245	9.6	200
3	Denman	1500	7	76	-18	0.006	1700	0.173	34	1000
4	Lambert	1100	22	5	-29	0.009	700	0.231	1.6	160
5	MacAyeal	1000	34	10	-26	0.002	400	0.054	2.9	78
6	Mellor	1200	10	3	-28	0.005	500	0.161	1.1	110
7	Pine Island	1500	22	77	-21	0.003	2600	0.075	34	1500
8	Recovery	2600	25	8	-32	0.001	300	0.107	6.1	82
9	Rutford	1700	13	39	-20	0.003	400	0.166	20	140
10	Slessor	1800	16	10	-26	0.005	400	0.298	5.3	120
11	Thwaites	1800	95	85	-21	0.003	800	0.142	45	360

Table 3: Parameter values from Quantartctica3 [Matsuoka et al., 2018] on 11 key ice streams. Columns left to right are thickness, ice stream half-width, average annual accumulation rate, average annual surface temperature, average surface slope, and stream center velocity near the grounding line. Also provided are the dimensionless Galilei (Ga), Péclet (Pe), and Brinkman (Br) numbers for each location.

bered on Fig. 3) with average annual surface temperatures -32°C to -18°C, average annual snow accumulation between 3 and 85 cm/yr, maximum downstream velocities of 300 $\mathrm{m\,yr^{-1}}$ to 2600 $\mathrm{m\,yr^{-1}}$, and average surface slopes approximately 0.001 to 0.009. Ice stream thickness and half-width are highly variable, leading to δ_z values ranging from 0.02 for Thwaites to 0.21 for Denman.

To explore a representative sample of model behavior, we simulate 6,000 unique scenarios, spanning the parameter space, on a 1km thick glacier with a constant 10km stream half-width (δ_z value: 0.1). We split the simulations between two different ridge geometries—10km and 20km wide—leading to δ_y values of 2 and 3 respectively. For each geometry we simulate five different stress scenarios: low driving stress ($\tau_d = \rho g H \sin\alpha$) with basal drag ($\tau_b = f_{\tau_b}\tau_d$) at 30% of driving; moderate driving stress with basal drag at 20%, 30%, and 40% of driving; and high driving stress with

basal drag at 30% of driving. These low, moderate, and high driving stress cases correspond to surface slopes of 0.002, 0.003, and 0.004 —approximately 18, 27, and 36 kPa—respectively. For each stress scenario we simulate accumulation rates in increments of 2 cm/yr between 2 cm/yr and 80 cm/yr and surface temperatures in one degree increments from -32°C to -18°C, hitting all possible combinations.

Our model solves for the temperature and velocity profiles of both the ice stream and its bordering ridge. To better visualize behavioral trends, we analyze the model using key nondimensional parameters, of which there are five (defined in Table 2): δ_z, `Ga`, `Br`, and `Pe` appear within the velocity and temperature equations (13) and (14), and δ_y manifests through equations (15) and (16) for advection. To best visualize the relation between shear heating and advection we present the results from our idealized study in `Br`-`Pe` space. From the definitions in Table 2, $\texttt{Pe} \propto \dot{a}$ so higher `Pe` corresponds to higher rates of advective cooling, while $\texttt{Br} \propto u_c^{4/3}(T_m - T_s)^{-1}$ so larger `Br` is favored by warmer surface temperatures and faster downstream velocities. Fig. 4 shows the temperate fraction (f_t)—the fraction of the total domain (stream and ridge) that is temperate—for each $(\texttt{Br}, \texttt{Pe})$ pair. The top row corresponds to $\delta_y = 2$ and the bottom row to $\delta_y = 3$. The order of columns is by increasing margin resistance or accommodated driving stress ($\tilde{\tau}_d = \tau_d\,[1 - f_{\tau_b}]$), as detailed above. The 6,000 forcing scenarios are equally distributed among the 10 panels, so the shape of each $(\texttt{Br}, \texttt{Pe})$ envelope emerges from 600 simulations.

Focusing first on the lowest accommodated driving stress regime (leftmost pan-

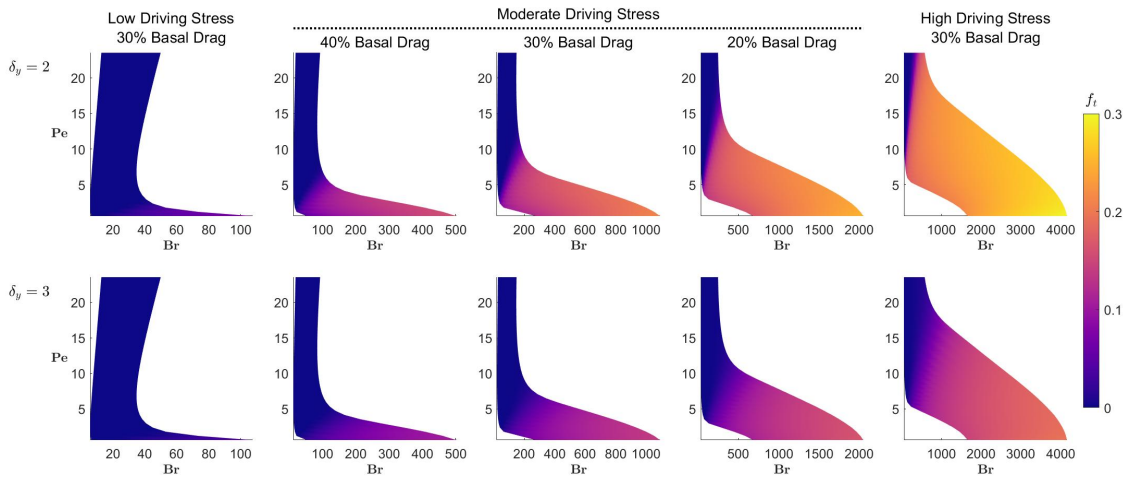

Figure 4: Temperate fraction (f_t) plotted in Br-Pe space. Each panel summarizes the findings from 600 steady-state simulations for the labeled stress regime, with effective driving stress $\mathtt{Ga}\,[1 - f_\tau]$ increasing left to right. The top row corresponds to $\delta_y = 2$, such that the ice ridge is the size of the ice stream half-width, while the bottom row corresponds to $\delta_y = 3$ with each ridge being equal in width to the entire ice stream. We see a large increase in Br immediately upon temperate onset, representative of high velocities when temperate ice is present.

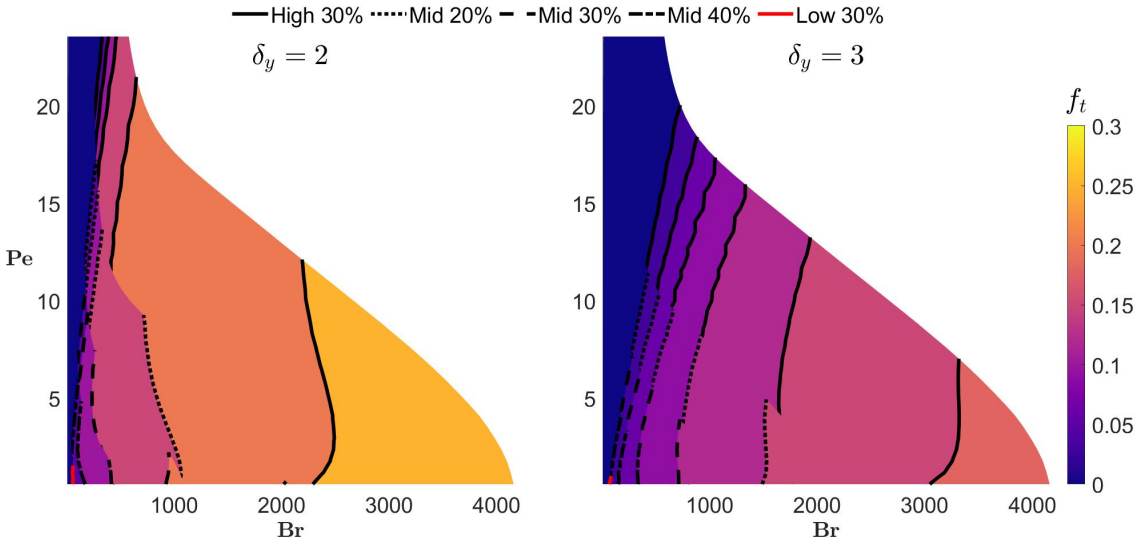

Figure 5: The plots from figure 5 overlaid on top of each other ($\delta_y = 2$ on the left, $\delta_y = 3$ on the right) in Br-Pe space. Each plot has a unique contour line style. We find each contour line is roughly continuous, an indicator that—for each set of geometric bounds—temperate volume is almost exclusively controlled by Pe and Br regardless of driving stress.

els) we find relatively low temperate fractions in all simulations. However, as soon as temperate ice is able to develop, we see large increases in Br, reflecting rapid velocity increases upon temperate onset; this behavior is favored particularly at low Pe (i.e. low $\dot{a}$) which mark conditions in which shear heating is dissipated primarily by conduction rather than lateral advection. We also note a secondary increase in Br that occurs at larger Pe, again suggesting an increase in velocity. We attribute this secondary increase to the presence of such large accumulation rates, that the ice stream must increase in speed to balance mass. The shape of the (Br, Pe) envelopes remain similar in the higher effective driving stress regimes. However, for the range of forcing conditions modeled here, under elevated driving stresses even the lowest $\dot{a}$ and coldest T_s ensure that the sliding speed is sufficiently rapid that the minimum Br is nonzero. We also see dramatic increases in temperate volume, reaching up to about 30% of the model domain. In all plots, we note that the location in Br-Pe space of the pink colored band, representing a temperate fraction of approximately 0.10, appears to be consistent throughout all five stress regimes. This is shown more clearly by an overlay of the plots (Fig. 5), where the line $f_t = 0.10$ is roughly continuous, suggesting temperate zone growth is most strongly controlled by Br and Pe for each ice stream geometry and is much less sensitive to driving stress.

Another window into the system behavior is given by a comparison between Brinkman and Galilei, both of which depend on maximum stream center velocity; $\mathtt{Ga} \propto u_c^{-1/n}$ and $\mathtt{Br} \propto u_c^{(n+1)/n}$. As noted above, our model solves for the velocity

profile of the ice stream and the Galilei and Brinkman numbers are determined as part of the simulation results. To explore the relation between these two parameters, we run a set of targeted parameter sweeps, where we alter only one parameter at a time—either `Pe`, δ_y, or δ_z—keeping the others constant while increasing surface slope. We first set a constant geometry ($\delta_y = 2, \delta_z = 0.1$) and simulate ten different Péclet values, each corresponding to a different accumulation rate. Our next set of simulations imposes constant Péclet, with δ_y varying in increments of 0.5 between 1.5 and 4.0, each simulating a unique ridge geometry. We then run a targeted sweep over fourteen δ_z values between 0.07 and 0.20. For each value of these parameters we run 31 simulations, varying surface slope ($\sin\alpha$) in 0.0001 increments between 0.001 and 0.004, the whole time holding the fractional basal friction constant at 30% of driving stress.

Results from each parameter set are found in Fig. 6, with filled circles representing simulations that produce temperate ice. We find there is a maximum value of `Ga` for each parameter choice, whereas `Br` increases steadily throughout. The maximum `Ga` value signifies a change in dominance between physical effects. At lower effective driving stresses an increase in surface slope produces a relatively small increase in velocity, such that the increase in surface slope dominates and `Ga` increases. However, at larger effective driving stresses, the same increase in surface slope leads to a much larger change in velocity that dominates the system, causing `Ga` to decrease. This behavioral change reflects pervasive margin softening that manifests close to the point

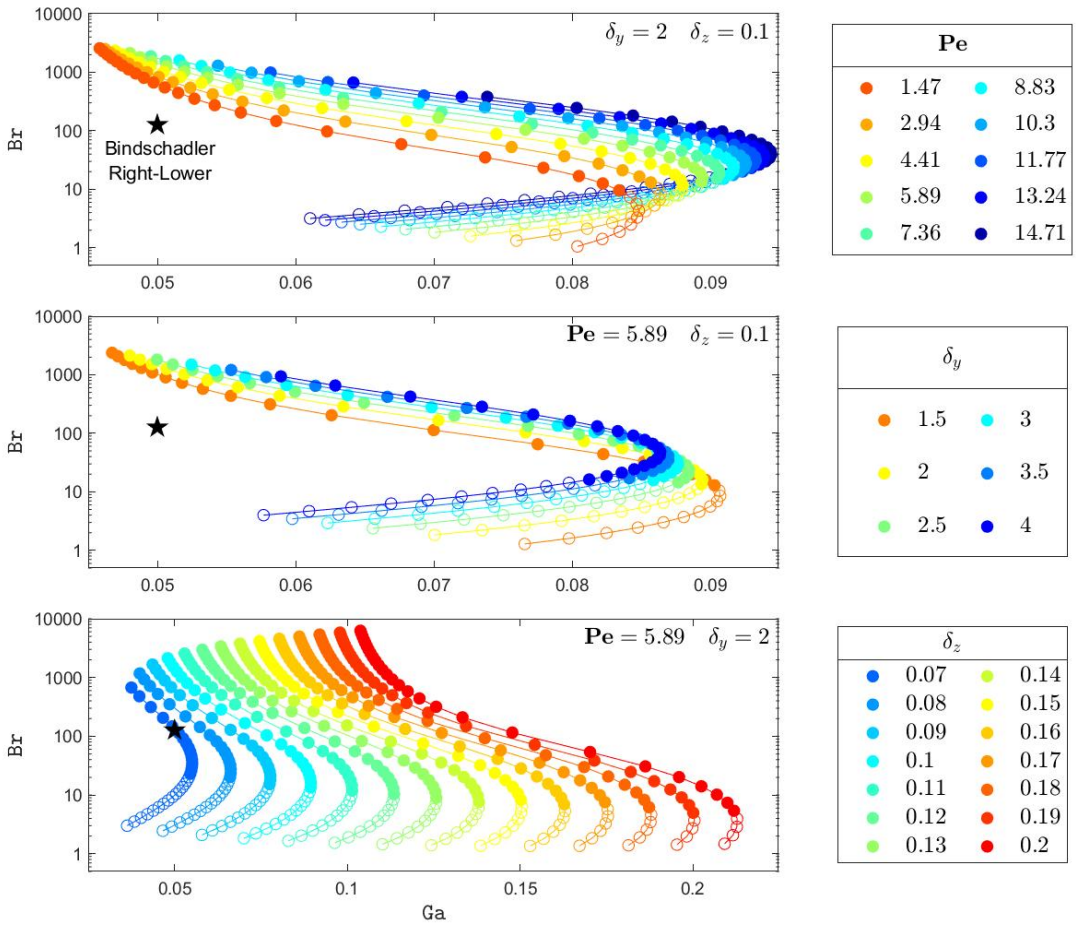

Figure 6: Results from a set of targeted parameter sweeps, where we alter only one parameter at a time—top to bottom `Pe`, δ_y, and δ_z—keeping the others constant while increasing surface slope. Each color represents a single value of the parameter with each data point a distinct surface slope. Simulations in which temperate ice develops are denoted by filled circles. Each parameter chosen has a maximum value of `Ga` that roughly corresponds to temperate onset. This maximum reflects pervasive margin softening that requires dramatic velocity increases to generate sufficient shear resistance that balances the difference between driving and basal stresses. For context to our later Bindschadler case study, the black star corresponds to the present day (`Ga`,`Br`) location for the cross-section Right-Lower.

at which temperate onset occurs, requiring dramatic speeds to develop and generate sufficient margin shear resistance to balance the difference between the driving and basal stresses.

To draw a direct relation between the nondimensional parameters and the onset of temperate ice we pick out the maximum Galilei value for each parameter set ($\mathtt{Ga}_{\max}$) and its corresponding Brinkman number ($\mathtt{Br}\,[\mathtt{Ga}_{\max}]$) and plot each as a function of the underlying parameter, either $\mathtt{Pe}$, δ_y, or δ_z, ultimately fitting a curve to the data points. The results are presented in Fig. 7, with the equation relating the two parameters as the title of each plot, and the R^2 value for each provided in the legend. We note that for low $\mathtt{Pe}$ and δ_y values, the onset of temperate ice occurs just after $\mathtt{Ga}_{\max}$ is reached, with the opposite for high $\mathtt{Pe}$ and δ_y; the same is true for high and low δ_z respectively (see Fig. 7). Our model resolution is sufficient to measure temperate fractions as low as 2.5×10^{-8} so the precise onset of temperate ice need not act like an abrupt mechanical switch, and the nearby peak $\mathtt{Ga}_{\max}$ that we focus on here is more diagnostic of changes in system behavior.

We do find strong correlations between the nondimensional parameters ($\mathtt{Pe}$, δ_y, δ_z) and the two values $\mathtt{Ga}_{\max}$ and $\mathtt{Br}\,[\mathtt{Ga}_{\max}]$. The curve fits in Fig. 8 suggest that the primary control on $\mathtt{Ga}_{\max}$ is δ_z—the ratio between ice thickness and stream half-width—and that the changes due to an increase in cold ice flux through the margin (i.e. increasing $\mathtt{Pe}$ or δ_y) are comparatively small. The value of $\mathtt{Ga}_{\max}$ increases linearly with δ_z ($R^2 = 1.000$), representative of a thicker ice stream having increased

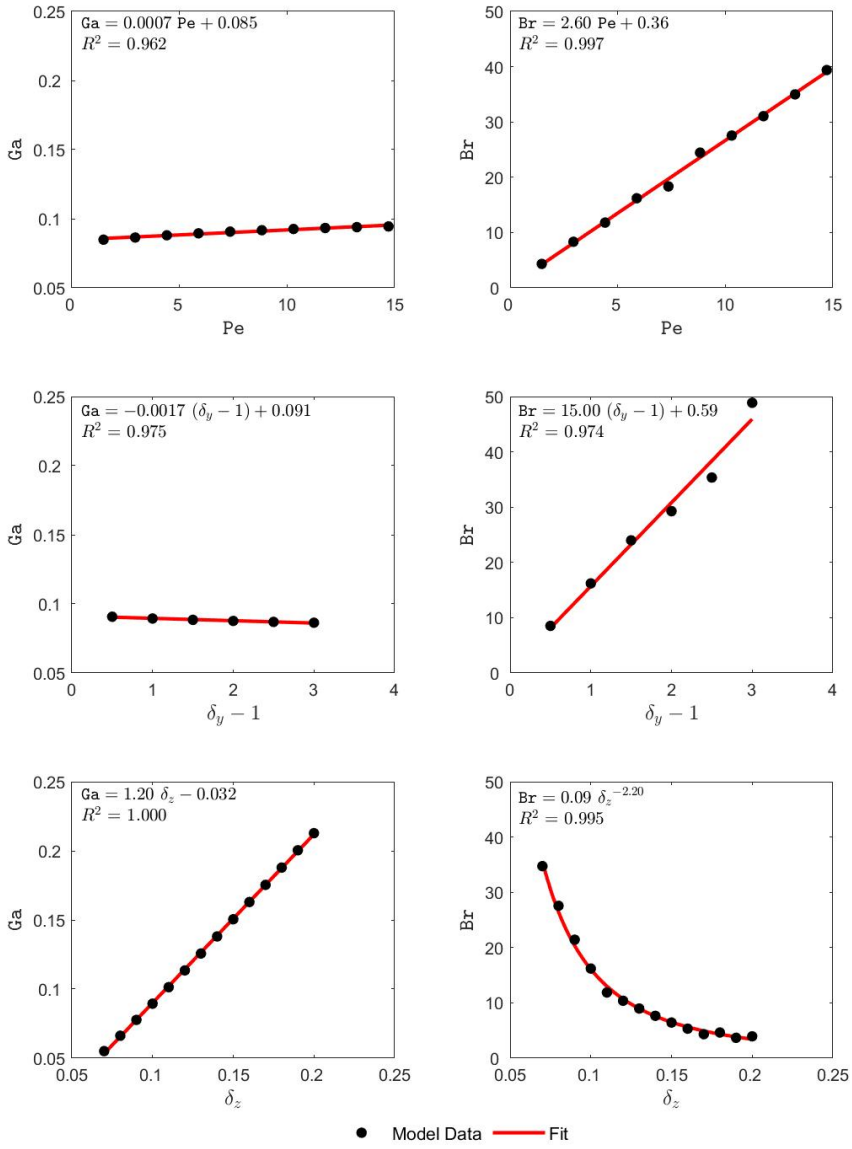

Figure 7: For each parameter detailed in Fig. 7 we extract the maximum Galilei value $\texttt{Ga}_{\max}$ and the corresponding Brinkman value $\texttt{Br}\,[\texttt{Ga}_{\max}]$, plot them independently, and look for trends in behavior. The title of each plot is the equation of its trend line, with the R^2 value provided in each panel. We interpret $\texttt{Ga}_{\max}$ as the minimum accommodated driving stress ($\tilde{\tau}_d = \tau_d\,[1 - f_{\tau_b}]$) most likely to produce temperate ice, and $\texttt{Br}\,[\texttt{Ga}_{\max}]$ as the shear resistance in the margin at that driving stress. As Pe increases, and a higher volume of cold ice advects through the margin, more shear resistance is required to produce temperate ice. This increased shear resistance requires higher driving stress. We see similar behavior when δ_y is increased, corresponding to a larger catchment area ($\delta_y - 1$) and an increase in advection through the margin; however, the higher shear resistance in this case requires slightly lower $\tilde{\tau}_d$. When δ_z is increased—here corresponding to increased ice thickness—less shear resistance is required, the result of ice lower in the column having greater insulation from surface temperatures. It does require higher $\tilde{\tau}_d$ to reach this point as a thicker ice column is better able to vertically distribute strain.

resistance to shear since depth-integrated resistance is directly proportional to ice thickness. We also see linear increases in the corresponding `Br` value needed to generate temperate ice when lateral advection is increased through `Pe` or increased ridge catchment size ($\delta_y - 1$), and a power law decrease in the `Br` value when thickness is increased (${\delta_z}^{-2.2}$). Overall, the results are consistent with expectations that as lateral advection increases, bringing more cold ridge ice towards the margin, the system requires greater shear heating to become temperate, whereas, a thicker ice stream will have a bed that is more insulated from the surface temperature, and therefore require less shear heating to develop temperate ice.

Application to Bindschadler Ice Stream

Having illustrated some of the key features of the system behavior, we next apply our model to a natural system that is well-characterized by the idealized geometry we consider: Bindschadler Ice Stream. Part of the Siple Coast, Bindschadler is an ideal candidate on which to test our model because it is mostly ridge-controlled—bordered by ice ridges of similar thickness to the ice stream, with constant bed elevation throughout—and has two distinct flow regimes: the upper section defined by a flatter surface and slower speeds, with the lower section having a steeper surface and faster speeds. We define the ridges for either side of the stream (denoted left and right) by highlighting areas where surface velocity trends towards the stream. We also take a lateral cross-section along the center of the stream from which surface slope is calculated.

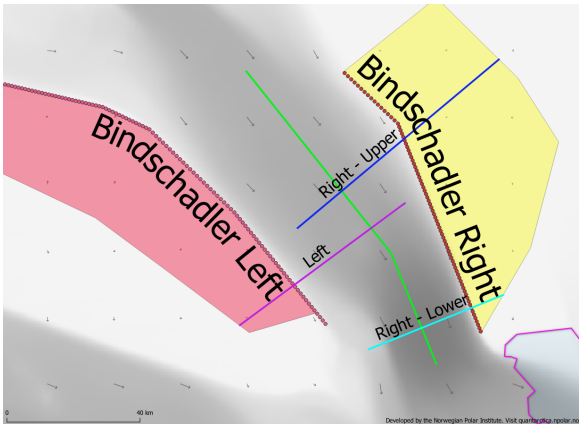

Figure 8: The three cross-sections (magenta, blue, and cyan) analyzed for our Bindschadler case study, with ridge systems denoted by the shaded polygons. The gray-scale and accompanying arrow surface show the magnitude and direction of surface velocity. The green line is the along-stream section from which we calculated surface slope and the dotted lines are estimated margin locations.

We run our model for three cross-sections, one through the left margin in the upper section, and two through the right margin—one in the upper section and the other in the lower. Fig. 8 depicts the catchment areas, the central flow-line (green), and the three cross sections analyzed—hereby referred to as "Left" (magenta), "Right-Upper" (blue), and "Right-Lower" (cyan).

With the same data sets used in the idealized stream study, we calculate the nondimensional parameters for all three cross-sections. Bindschadler is a relatively consistent thickness along its entire length and the accumulation rate is nearly constant, so `Pe` is ~ 2 for all sections, whereas the changing slope causes a 30% increase in `Ga` from 0.038 in the upper region to 0.050 in the lower. Enhanced shear leads to a 60% increase in `Br` from the upper to lower section, with values of 84, 70, and 127 for Left, Right-Upper, and Right-Lower respectively. The stream narrows from ~ 30 km half-width in the upper section to ~ 15 km in the lower section, but the ridge system

shrinks even more dramatically, leading to a steady decrease in δ_y downstream. The right ridge is larger than the left in the upper section and we approximate $\delta_y = 1.6$ for Left and Right-Lower, and $\delta_y = 2.3$ for Right-Upper. The decreasing stream width at constant thickness leads to a doubling of δ_z in the lower section, from 0.03 to 0.06. All of these factors combine to provide a comprehensive suite of parameters that is amenable for further analysis with our model. For each cross-section we run five different climate conditions, the first being present day, while the other two represent predicted conditions for the years 2100 and 2300 using emissions scenarios RCP 4.5 and RCP 8.5. For context into how the Bindschadler study relates to the idealized simulations, the present day conditions for Right-Lower are depicted with a black star in Fig. 6. We match the stream center velocity by adjusting the basal friction τ_b which is our only free parameter.

Our results from the present day study are depicted in Fig. 9. For each cross-section we provide the surface velocity—modeled is the solid black line and measured is the dashed colored line [Rignot et al., 2011; Mouginot et al., 2012], as well as the temperature profile and the surface strain rate. Overall, we find the surface velocity profiles returned by our model closely resemble the measured velocities. Right-Lower is the only section predicted to have temperate ice ($f_t \approx 0.05$), and we note a distinct peak in strain rate corresponding to the location of maximum temperate zone thickness. This peak is displaced slightly from the slip/no-slip transition into the more rapidly flowing stream. By contrast, in the sections without temperate ice we find the

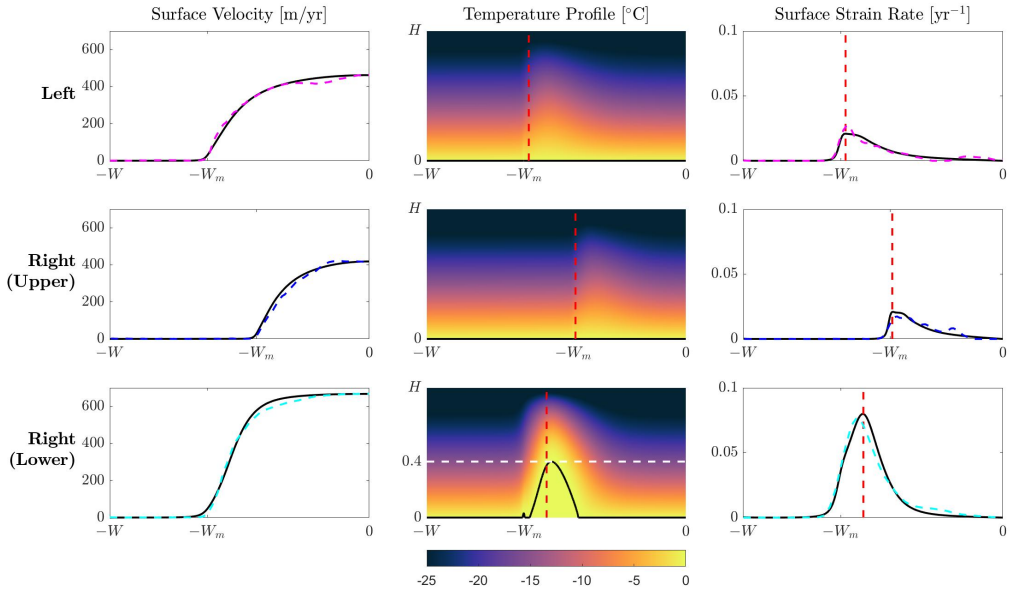

Figure 9: Bindschadler case study results. Column 1: Modeled surface velocity (solid black line) plotted alongside measured surface velocity (colored dashed lines). Column 2: Cross-sectional temperature profile with thick black contour indicating temperate ice region. Red dashed lines show the location of maximum surface strain rate. The white dashed line on the lower profile corresponds to maximum temperate extent. Column 3: Modeled surface strain rates with location of maximum strain in red. There is a noticeable spike in surface strain when temperate ice is present roughly corresponding to the location of maximum temperate extent. When temperate ice is absent the strain-rate distribution is approximately even across the shear margin.

strain rate is distributed much more evenly across the margin, though still with a clear correlation between elevated strain rates and higher temperatures. We also note, in Right-Lower, a small temperate zone at the slip/no-slip transition ($|y| = W_m$) that is distinct from the main temperate zone. This behavior is reminiscent of other studies modeling ice stream behavior (e.g. Suckale et al. [2014]; Haseloff et al. [2019]). There is low advective cooling near the slip/no-slip transition point, meaning it should be easier for temperate ice to develop just above the bed in the region very close to the ridge. However, in our idealized model formulation this also represents an integrable stress singularity with associated unphysically large concentrated heat input [e.g. Perol et al., 2015]. Numerical tests confirm that although the calculated localized melting rate increases with grid refinement, the predicted volume flux remains negligible and the predicted ice velocity and temperature fields away from this singular point are not sensitive to grid refinement. A more robust discussion of the singularity is found in the supplemental materials.

We are interested not only in the locations of temperate ice in Bindschadler, but also in the effect temperate ice has on melt distribution to the bed. We present the combined melt rates (shear and basal) along the bed for the three cross-sections analyzed in Fig. 10. The black lines are present day, and the blue dashed and red dotted lines are for altered model forcings chosen to correspond with forecasts for two future greenhouse gas emissions scenarios. We approximate the basal melt rate by taking the total heat input from frictional sliding and dividing by latent heat. Hence, any

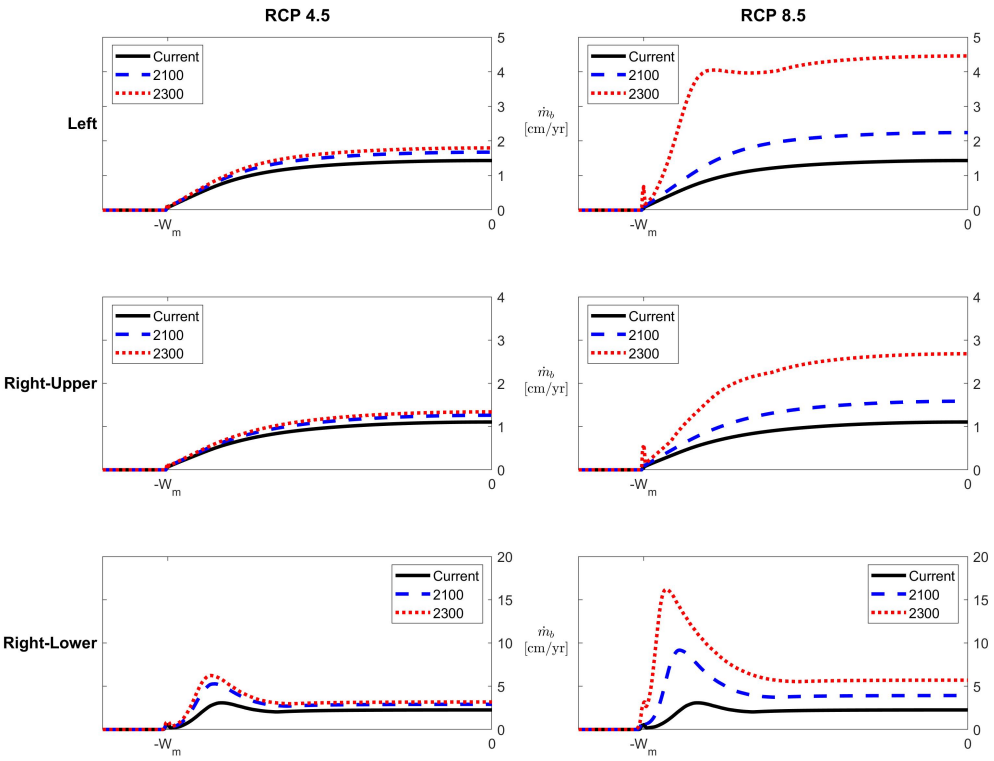

Figure 10: Steady-state basal melt distribution for Bindschadler under conditions predicted by emissions scenarios RCP 4.5 (left) and RCP 8.5 (right). The top row is the Left cross-section, the middle row is Right-Upper, and the bottom is Right-Lower. On all plots the black line (solid) represents present day conditions, the blue line (dashed) is under year 2100 predictions, and the red line (dotted) is under year 2300 predictions. A peak in melt near $|y| = W_m$ suggests the presence of temperate ice, whereas an increase in melt further into the stream suggests higher velocities causing greater frictional melting at the bed. The thin spikes just above W_m are a likely model artifact that, when melt is integrated laterally across the stream, are negligible. While basal melt increases under RCP 4.5 conditions at all years are relatively minor, under the RCP 8.5 scenario increases are drastic, up to an approximate 250% increase in total basal melt for the Left and Right-Lower sections by year 2300. For more detail see table 5.

difference between the input geothermal heating and conductive transport towards the glacier surface is neglected, both to remove uncertainties in the former and to better focus on the effects of dissipative heating, while ignoring the small changes that arise directly from differences in surface temperature conditions. To facilitate this comparison, consistent with our steady-state treatment, we assume that the rate of melt production within the temperate ice is matched by the rate of meltwater supply to the bed immediately below. Of course, in the absence of temperate ice, as is the case for Left and Right-Upper, there is no shear melting, and all meltwater is created by friction from sliding at the bed. In such cases the greatest melt rates are found towards the center of the stream where the flow speed is fastest. In the case where temperate ice is present (Right-Lower) we find shear melting adds considerable melt to the ice close to the margin beneath the slower moving ice, with potential implications for the distribution of basal strength [Perol et al., 2015; Meyer et al., 2018].

Impact of a Warming Climate

To extend our Bindschadler case study we analyze the temperate fraction and meltwater production for the same three cross-sections under predicted polar temperatures at the years 2100 and 2300. We use data from CMIP5 extrapolated to 2300 by Bulthuis et al. [2019] under both the RCP 4.5 and RCP 8.5 emissions scenarios. RCP 4.5 predicts a surface temperature increase of 1.6°C by 2100 and 2.3°C at 2300. RCP

8.5 implies much higher temperatures, with a 4.2°C increase by 2100 and 9°C at 2300. Additionally, we assume each 1°C temperature increase is accompanied by a 5% increase in annual precipitation, consistent with climate predictions with CMIP5 presented by Golledge et al. [2015]. Beyond surface temperature and precipitation rate, we do not take into consideration any other factors that may impact glacial flow such as ice sheet thinning, ice shelf melting, ice stream width changes, grounding line retreat, or basal weakening. Instead, we simply take Bindschadler Ice Stream, as it appears today, place it into conditions consistent with the climate change predictions, and run the model to steady-state—a simplification that allows for direct comparison between all three sets of simulations.

These elevated temperatures and accompanying accumulation rates correspond to relatively small increases in `Pe`, from about 2 for all cross-sections at present day to 2.3 at year 2300 using RCP 4.5 and 3 with RCP 8.5. Upon reaching steady state, increased stream center velocity causes modest decreases in `Ga` ($\sim 10\%$) under RCP

Scenario	**Year**	**Left**			**Right-Upper**			**Right-Lower**		
		`Pe`	`Ga`	`Br`	`Pe`	`Ga`	`Br`	`Pe`	`Ga`	`Br`
Present Day		2.1	0.038	84	1.9	0.038	70	2.0	0.050	127
RCP 4.5	2100	2.3	0.036	110	2.1	0.036	88	2.2	0.046	188
	2300	2.4	0.035	124	2.1	0.035	98	2.3	0.045	306
RCP 8.5	2100	2.6	0.033	180	2.3	0.034	132	2.4	0.042	310
	2300	3.1	0.026	402	2.8	0.028	331	2.9	0.037	630

Table 4: Predicted `Pe`, `Ga`, and `Br` values for the three representative Bindschadler cross-sections under emissions scenarios RCP 4.5 and RCP 8.5 at the years 2100 and 2300. All simulations assume the same glacier geometry as present day, and are run to steady-state.

4.5 and about a 25% reduction using RCP 8.5. These Ga decreases stem from centerline velocity increases of 30-40% for RCP 4.5 and 150-200% for RCP 8.5, and assume basal friction remains consistent with present day estimates. Changes in Br are much more pronounced than those of Ga, with Left and Right-Upper showing increases of 40% under RCP 4.5 and Right-Lower showing a 140% increase at 2300. Under RCP 8.5 conditions, all three cross-sections show an increase to Br in excess of 350%, topping out at nearly 400% for Right-Lower. More detail on how Pe, Ga, and Br vary under each scenario is found in Table 4. The forecast trend in all of these scenarios is for relatively small changes in Pe and Ga in comparison to much larger changes in Br, suggesting a considerably higher propensity for temperate zone formation (i.e. recall from Fig 7 that the threshold Br for temperate onset changes only linearly with Pe).

We are also interested in how the massive increases in shear heating under these conditions equate to changing melt distributions at the bed. Fig. 10 shows the predicted melt distribution for each cross-section under both climate change scenarios, along with comparisons to model results under current conditions. A peak in meltwater distribution near the margin ($|y| = W_m$) can be attributed to shear melting within a temperate ice zone, whereas increased melting near the stream center ($y = 0$) represents enhanced frictional melting due to increased sliding speed. A more detailed comparison between the basal and shear melt components for each scenario can be found in Table 5, with temperature profiles of each cross-section reserved for the supplemental materials. Under RCP 4.5 conditions Bindschadler remains relatively

Year	Melt [m^2/yr]	Left		Right-Upper		Right-Lower	
		RCP 4.5	RCP 8.5	RCP 4.5	RCP 8.5	RCP 4.5	RCP 8.5
Present Day	Basal	386		239		279	
	Shear	0		0		40	
	Combined	386		239		319	
2100	Basal	451	605	273	345	361	488
	Shear	0	0	0	0	86	173
	Combined	451 (17%)	605 (57%)	273 (14%)	345 (44%)	447 (40%)	661 (108%)
2300	Basal	485	1205	291	582	394	713
	Shear	0	98	0	9	107	355
	Combined	485 (26%)	1303 (238%)	291 (22%)	591 (147%)	501 (57%)	1068 (235%)

Table 5: Shear, basal, and combined melt rates under emissions scenarios RCP 4.5 and RCP 8.5 integrated along the bed of the three Bindschadler cross sections analyzed. Percentage increases in total melt rate from present day are given in parentheses.

similar to present day in the upper section however, the lower region shows a nearly 100% increase in shear melting by 2100 and a 150% increase by 2300.

The RCP 8.5 simulations are, as expected, much more striking. Not only do all three cross-sections develop temperate ice under 2300 conditions, but they also show a significant velocity increase. For instance, Left, which shows no temperate ice under year 2100 conditions, nearly doubles in velocity, and its total melt rate increases by over 50%. Using conditions predicted in 2300 the left shear margin has a significant temperate zone, and experiences shear melting at a rate that is more than double that of Right-Lower under current conditions, with a 230% increase in total melt rate. Right-Upper undergoes the least amount of change, developing a relatively small temperate zone under 2300 conditions, but its total melt rate still increases by nearly 150%, mainly due to enhanced basal melting. Right-Lower undergoes the most significant changes, with considerably more temperate ice developing along the

outer edge of the shear margin. When using the 2100 predicted conditions, there is a near 300% increase in shear melting, and a doubling of total melt. Under the 2300 conditions shear melting increases by more than 750%, and total melt more than triples when compared to present day.

IV DISCUSSION

We quantify the effects of lateral advection on ice stream thermomechanics using a two-dimensional (three velocity component) steady-state model applied to a suite of idealized ice streams and one designed to simulate three representative cross-sections thorugh Bindschadler ice stream. Using a steady-state model is computationally feasible for running through a broad swath of parameter space by avoiding the need to integrate over long time scales needed for significant changes in ice stream behavior, as well as the uncertainty involved in assigning evolving forcing conditions. It also gives us a good sense for the dominant behavior when minor changes in atmospheric conditions are detected, for which we have a very short instrumental record. While there is potential to expand this model to use in a time-dependent study, this expansion would benefit from a better understanding of ice stream widening and margin migration as well as the effects of other important processes that we exclude from our analysis, such as fabric development [e.g. Ranganathan et al., 2020]. For our purposes, given the current glaciological knowledge base, a steady-state model formulation has the advantage of providing a more focused platform for making concise comparisons between simulations than would its more complex time-dependent counterpart.

To facilitate direct comparisons between dominant forces and exclude cases that may be physically different, but systemically the same, we utilize nondimensional parameters. We compare the rates of advective cooling through the dimensionless Péclet number (`Pe`) and gauge responses in the ice stream through the nondimen-

sional Galilei (Ga) and Brinkman (Br) numbers. We have demonstrated that for each individual parameter set there exists a maximum Galilei value $\mathtt{Ga}_{\max}$ that roughly corresponds to temperate onset within the margin ice and effectively marks a shift in shear margin behavior from cold and rigid, to warm and soft. The softer ice is able to accommodate much higher strain rates as driving stress increases require accompanying lateral stress increases in the margin to balance forces. Though higher Pe values require slight increases in downstream forcing to initiate temperate onset (i.e. $\mathtt{Ga}_{\max}$ remains relatively constant), the required shear heating increases—manifest through $\mathtt{Br}\,[\mathtt{Ga}_{\max}]$—are significantly larger, and the dependence on Pe is linear.

We analyze the same thermomechanical properties through various ice stream geometries, first using a suite of ridge extents through the dimensionless parameter δ_y and then with changing ice thickness, nondimensionalized with δ_z. We find an increase in δ_y—corresponding to a larger ridge catchment area—acts similarly to an increase in Pe with $\mathtt{Br}\,[\mathtt{Ga}_{\max}] \propto (\delta_y - 1)$, where $(\delta_y - 1)$ is the nondimensional ridge width. This behavior is to be expected, as an increased catchment size requires higher advection rates through the margin to balance mass within the ridge (see eq. 15). Interestingly, the value $\mathtt{Ga}_{\max}$ reduces with δ_y logarithmically, though the magnitudes of driving stress decreases are minimal. We attribute this strange behavior to the ridge extent increase causing the ridge to stiffen near the margin, forcing more shear within the margin, and leading to higher shear heating at lower velocities. In contrast, when the ice thickness is increased, corresponding to an increase in δ_z, higher

velocities are required to form temperate ice, and thus $\mathtt{Ga}_{\max}$ also increases. This relation is nearly perfectly linear ($R^2 = 1.000$). We also see a power-law decrease in $\mathtt{Br}\,[\mathtt{Ga}_{\max}]$ when δ_z increases, an indication that lower strain rates are required to form temperate ice in thicker streams. Lower strain rates occurring at higher velocities in thicker ice streams is due to thicker streams having a larger vertical extent over which to distribute shear, thus requiring a higher stream velocity in order to reach similar strain rates to its thinner counterparts. Less shear heating being required to form temperate ice as δ_z increases is an indicator that the bed of the thicker ice stream is more insulated from the cold surface.

To see how these dominant behaviors manifest within a natural system, we test our model on Bindschadler Ice Stream, considering three specific cross-sections. We predict temperate ice only in the section furthest downstream, consistent with results presented by Meyer et al. [2018]. From the temperate zone we are able to extract an approximate shear melt rate as well as a basal melt rate from the along-bed velocity profile. This allows for comparison between the meltwater distribution with and without shear melt, a comparison that supports the claims by Jacobson and Raymond [1998] that in the absence of temperate ice, meltwater is generated near the stream center, where velocities are faster, but that when a significant temperate zone develops a large volume of meltwater may be distributed below the slower moving ice, which they hypothesized could lead to ice stream widening [e.g. Haseloff et al., 2018]. However, we note that gradients in surface and bed topography along with

other sources of hydraulic complexity, that are not considered here, could help to distribute the meltwater and either mitigate or enhance the effects of excess melt in the subglacial system [Schoof, 2010; Meyer et al., 2018].

As a final model illustration, we expand upon our study by utilizing climate forecasts from CMIP 5 emissions scenarios RCP 4.5 and RCP 8.5. Both scenarios forecast a warming climate over at least the next few centuries, promoting temperate ice development. However, this temperature increase is expected to be accompanied by an increase in snow accumulation rate, thus increasing lateral advection rates. When running our model to steady-state for all three Bindschadler cross-sections under conditions expected using RCP 4.5 we see comparatively modest changes in melt rate—about 20% in the upper section and around 60% in the lower at the year 2300. Under the conditions predicted by RCP 8.5 in 2300 the situation becomes much more dire, with an average increase in melt rate of over 200%. In the lower section this equates to a 760% increase in shear melt rate alone, with a corresponding 150% increase in basal melt. A focussed influx of meltwater near the shear margin could promote channelized drainage and have a significant influence on basal effective stress distribution and associated basal resistance [e.g. Meyer et al., 2018]. Moreover, the discharge of such channels at the grounding line has been shown to promote the development of buoyant plumes in the water column [Jenkins, 2011; Carroll et al., 2015; Sutherland et al., 2019]. These freshwater plumes are expected to entrain warm, salty bottom water and promote melting as they rise against the ice shelf surface, with im-

plications for grounding line motion and ice shelf stability [Weertman, 1974; Schoof, 2007; Goldberg et al., 2009].

V CONCLUSIONS

In this study we develop a quasi-three-dimensional steady-state model for ice stream thermomechanics that couples temperature-dependent rheology to strain-rate-dependent shear heating. We consider a realistic natural range of lateral advection rates through an idealized ice stream shear margin, and pinpoint changes in behavior using dimensionless parameters, representative of competing forces throughout the domain. We use various modern Antarctic data sets to inform parameter choices [Rignot et al., 2011; Mouginot et al., 2012; Fretwell et al., 2013; Van Wessem et al., 2014; Matsuoka et al., 2018] and simulate 6,000 unique scenarios to gain insight into trends in behavior. A set of targeted parameter sweeps allows us to clearly see a shift in ice stream behavior from cold and slow to warm and fast; as expected, this behavioral change manifests near the onset of temperate ice development. The relation has three key contributors: accumulation rate, ridge catchment extent, and ice stream thickness. The first two factors—accumulation rate and ridge extent—are a control on shear warming as quantified through a linear relationship with the Brinkman number (`Br`)—the ratio of shear heating to thermal conduction—in that higher advection rates (or, alternatively, wider ridges) require more shear to develop temperate ice. This behavior is reminiscent of a cooling margin as more cold ice is supplied to the stream in order to balance mass in the ridge. Ice stream thickness is the main control on the downstream forcing required to produce temperate ice, as a thicker stream has a longer vertical extent over which to distribute shear resistance. This behavior

appears as a linear relationship with the required Galilei number—the ratio of gravitational and viscous forcing (`Ga`)—for temperate ice development.

To test our model in a natural setting we look to Bindschadler ice stream, and run our model for conditions chosen as representative of three specific cross-sections therein. Not only do the results for each section correspond well to measured results and previous studies [i.e. Meyer and Minchew, 2018; Meyer et al., 2018], but we also see temperate ice develop only under conditions expected by our own idealized study. To further reveal natural trends we utilize future climate predictions for surface temperature and corresponding snow accumulation increases [Golledge et al., 2015; Bulthuis et al., 2019] and run Bindschadler, as it appears today, to steady state under these future conditions. We find the two cross-sections further upstream shift from being cold and stiff to warm and soft, whereas the section furthest downstream, which is already expected to contain temperate ice, sees a large increase in temperate volume, and a nearly 750% increase in shear melting. Without accounting for potential changes in geometry or other forcing conditions beyond accumulation rate and surface temperature, we estimate total meltwater production increases for all three cross-sections by at least 350% under these future conditions, with a corresponding center-line velocity speed-up of nearly 200%. An increase in shear melt rate has been hypothesized to lead to ice stream widening as a large volume of meltwater is distributed to the bed directly below slower moving ice [Jacobson and Raymond, 1998; Haseloff et al., 2019]. An increase in basal meltwater near the shear margin could

alter the distribution of bed strength [Meyer et al., 2018] and, upon discharge to the ocean, might serve to promote circulation and melting [Sutherland et al., 2019], potentially affecting grounding line stability and forecasts for sea level change [Pegler, 2018].

A EXPANDED ADVECTION DERIVATION

Haseloff et al. [2019], as part of their extended ice stream model, present an approximation for in-plane lateral and vertical advection from a supplying ice ridge on a two-dimensional cross-section of variable thickness. This approach approximates these smaller velocity components effectively, thereby significantly simplifying numerical computations. However, in our model we prefer a constant thickness throughout the domain, so we adapt the advection approximation to fit our model geometry accordingly. We begin by defining our constant thickness H and use the same approximation to downstream velocity found in Haseloff et al. [2019] as

$$u \approx \begin{cases} u_c \left[1 - \left(\dfrac{y}{W_m} \right)^{n+1} \right] & |y| \leq W_m \\ 0 & W_m \leq |y| \leq W. \end{cases} \tag{A1}$$

With constant thickness we apply a depth-averaged mass conservation

$$\frac{\partial u}{\partial x} + \frac{\partial \bar{v}}{\partial y} = \frac{\dot{a}}{H} \tag{A2}$$

where $\dot{a}$ is accumulation rate and v is across-stream velocity (lateral advection). We can now integrate for the stream ($0 \leq |y| \leq W_m$) and ridge ($W_m \leq |y| \leq W$) separately by substituting in (S1) for u and integrating over the negative half of the

domain

$$\begin{cases} \displaystyle\int_0^y \frac{\partial \bar{v}}{\partial y}\,\mathrm{d}y = \int_0^y \frac{\dot{a}}{H}\,\mathrm{d}y - \int_0^y \frac{\partial}{\partial x}\left(u_c\left[1-\left(\frac{y}{W_m}\right)^{n+1}\right]\right)\,\mathrm{d}y & 0 \le |y| \le W_m \\ \displaystyle\int_y^{-W} \frac{\partial \bar{v}}{\partial y}\,\mathrm{d}y = \int_y^{-W} \frac{\dot{a}}{H}\,\mathrm{d}y & W_m \le |y| \le W, \end{cases} \tag{A3}$$

becoming

$$\bar{v} = \frac{\dot{a}}{H}y - \begin{cases} \dfrac{\partial u_c}{\partial x}\left[y - y\dfrac{1}{n+2}\left(\dfrac{y}{W_m}\right)^{n+1}\right] & 0 \le |y| \le W_m \\ -W & W_m \le |y| \le W. \end{cases} \tag{A4}$$

We enforce continuity at $|y| = W_m$ and generalize for any $0 \le |y| \le W$ to yield

$$\bar{v} = \frac{\dot{a}}{H}\begin{cases} y - \dfrac{n+2}{n+1}\dfrac{W}{W_m}y\left[1-\dfrac{1}{n+2}\left(\dfrac{y}{W_m}\right)^{n+1}\right] & |y| \le W_m \\ -\dfrac{y}{|y|}\left(W - |y|\right) & W_m \le |y| \le W, \end{cases} \tag{A5}$$

then we apply the shallow ice profile for the ridge to give the expression for lateral advection as

$$v = \frac{\dot{a}}{H}\begin{cases} y - \dfrac{n+2}{n+1}\dfrac{W}{W_m}y\left[1-\dfrac{1}{n+2}\left(\dfrac{y}{W_m}\right)^{n+1}\right] & |y| \le W_m \\ -\dfrac{n+2}{n+1}\dfrac{y}{|y|}\left(W - |y|\right)\left[1-\left(1-\dfrac{z}{H}\right)^{n+1}\right] & W_m \le |y| \le W. \end{cases} \tag{A6}$$

The expression for vertical advection is achieved through conservation of mass (e.g. eq (1) from the main text) and is found to be

$$w = \dot{a} \begin{cases} -\dfrac{z}{H} & |y| \leq W_m \\ -\dfrac{n+2}{n+1}\dfrac{z}{H} + \dfrac{1}{n+1}\left[1 - \left(1 - \dfrac{z}{H}\right)^{n+2}\right] & W_m \leq |y| \leq W. \end{cases} \tag{A7}$$

B RESOLUTION ANALYSIS

To ensure accuracy of our model we focus on the slip/no-slip transition point along the bed, which is the only discontinuity in our model domain. We want to ensure that the discontinuity is resolved well enough to converge, but that the mesh is not so dense as to be too computationally expensive. To test accuracy we looked at a series of built-in and custom resolutions. To illustrate this we pick three different resolutions, a low resolution (minimum element size 2×10^{-5}, maximum size 6.4×10^{-3}), a high resolution ($5{\times}10^{-6}$ minimum, $1.6{\times}10^{-3}$ maximum), and a variable resolution ($1{\times}10^{-5}$ minimum, 1×10^{-2} maximum). For the low and high resolution cases we allow COMSOL to choose the resolution throughout the domain, and in the variable case we force higher resolution near the discontinuity. For each resolution, we run a simulation on a model geometry from our Bindschadler case study (Right-Upper) under RCP 8.5 conditions predicted at year 2300. This simulation is useful for a resolution analysis because we do not expect to see temperate ice at the slip/no-slip boundary in this case, but the strain rates under these conditions are high enough to give the appearance of temperate ice having been produced at this point.

To get the shear melt-rate profile for each simulation we extract the data from the model, which is given as three column vectors—one for y, one for z, and the last for the shear melt rate $\dot{m}_s$—and cast this to a regular grid, which can then be integrated vertically for basal melt distribution, and both laterally and vertically for total meltwater supply. We utilize interpolation techniques to get values within the

Figure B1: Shear melt rates from the Right-Upper cross section of Bindschadler under emissions scenario RCP 8.5 conditions predicted in 2300. The top image is zoomed into the slip/no-slip transition with 250 m on either side of the singularity, and a vertical extent of 250 m shown. We would not expect to see temperate ice in this region under these conditions, however, when the data is interpolated we do see shear melting. When vertically integrated these interpolated values give non-negligible shear melt rates. To remedy this we instead use a moving average over 200m increments for shear melt rate only (as opposed to melting from friction along the bed). We also give the shear melt rate, integrated laterally across this 500m region, suggesting that even with high resolution, the singularity is integrable and provides a relatively small amount of meltwater to the subglacial system.

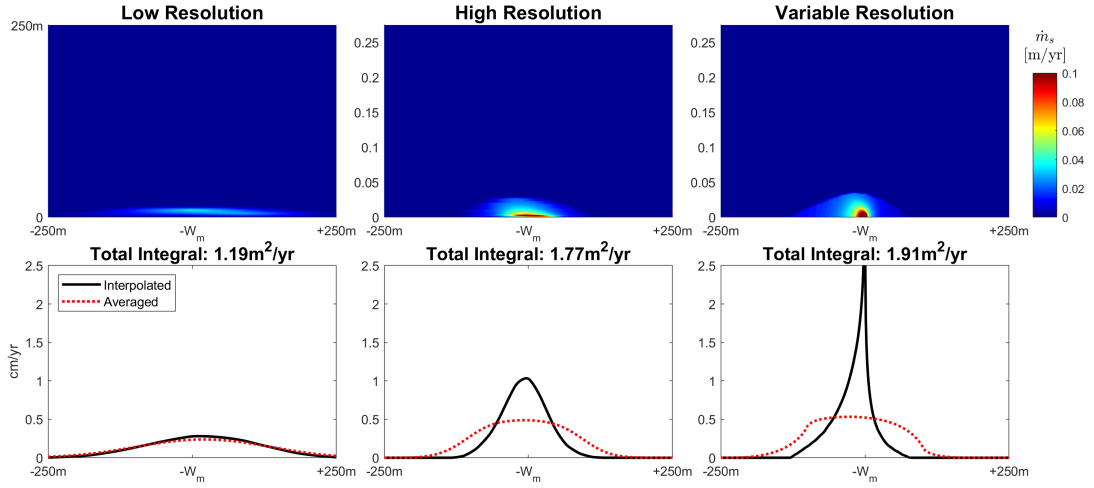

domain, but this only works for grid points sufficiently far from the stress singularity. As seen in Fig. B1, where the top row is a natural interpolation (continuous under differentiation), the high strain rates from the singularity behaves like a small, non-negligible temperate ice zone. When the values are integrated vertically to get a melt distribution rate at the bed (shown in Fig B1, bottom row, solid black line) we see melt rates upwards of 2 cm/yr, which is comparable to the total melt distribution rates given in Fig. 10 of the main text. These values result from high strain-rates near an integrable singularity that is characterized by a finite heat flux. To reduce model sensitivity to grid resolution near the singularity, we calculate moving averages over a fixed 200m horizontal dimension, providing more representative melt rates shown with the red lines in the bottom row of Fig. S1. As expected, we find that the rate of melt input at the slip/no-slip boundary is relatively small, and the total melt production near the singularity is nearly independent of the grid resolution. When the same averaging procedure is followed away from the slip/no-slip transition, the results are identical to the interpolated values.

C BIS TEMPERATURE PROFILES

In Fig. D1-D3 we show the predicted temperature field for the Bindschadler inspired model runs described in the main text.

Figure C1: Modeled temperature profiles for the Bindschadler cross-section labeled "Left" on Fig. 4 from the main text under various climate forcings. The top row is under present day conditions, the middle row uses predicted conditions at year 2100 under emissions scenairos RCP 4.5 (left) and RCP 8.5 (right), and the bottom row are the same emissions scenarios forecast to 2300. The black solid line corresponds to the 0°C contour.

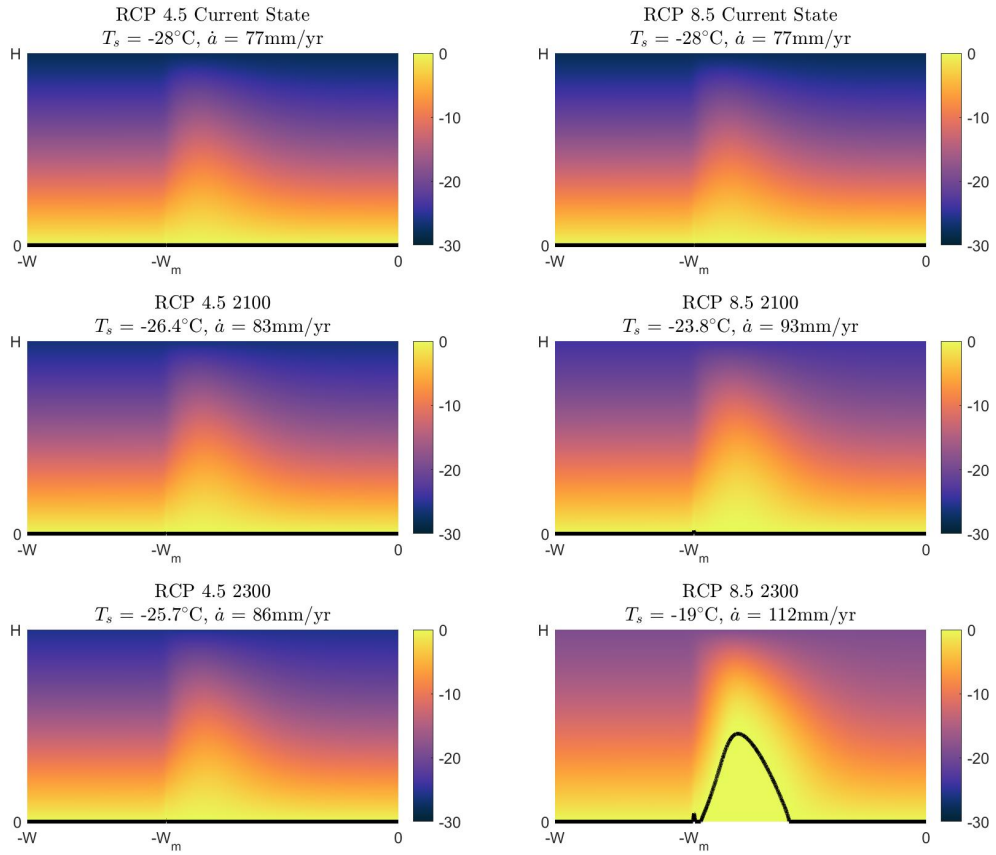

Figure C2: Modeled temperature profiles for the Bindschadler cross-section labeled "Right-Upper" on Fig. 4 from the main text under various climate forcings. The top row is under present day conditions, the middle row uses predicted conditions at year 2100 under emissions scenairos RCP 4.5 (left) and RCP 8.5 (right), and the bottom row are the same emissions scenarios forecast to 2300. The black solid line corresponds to the 0°C contour.

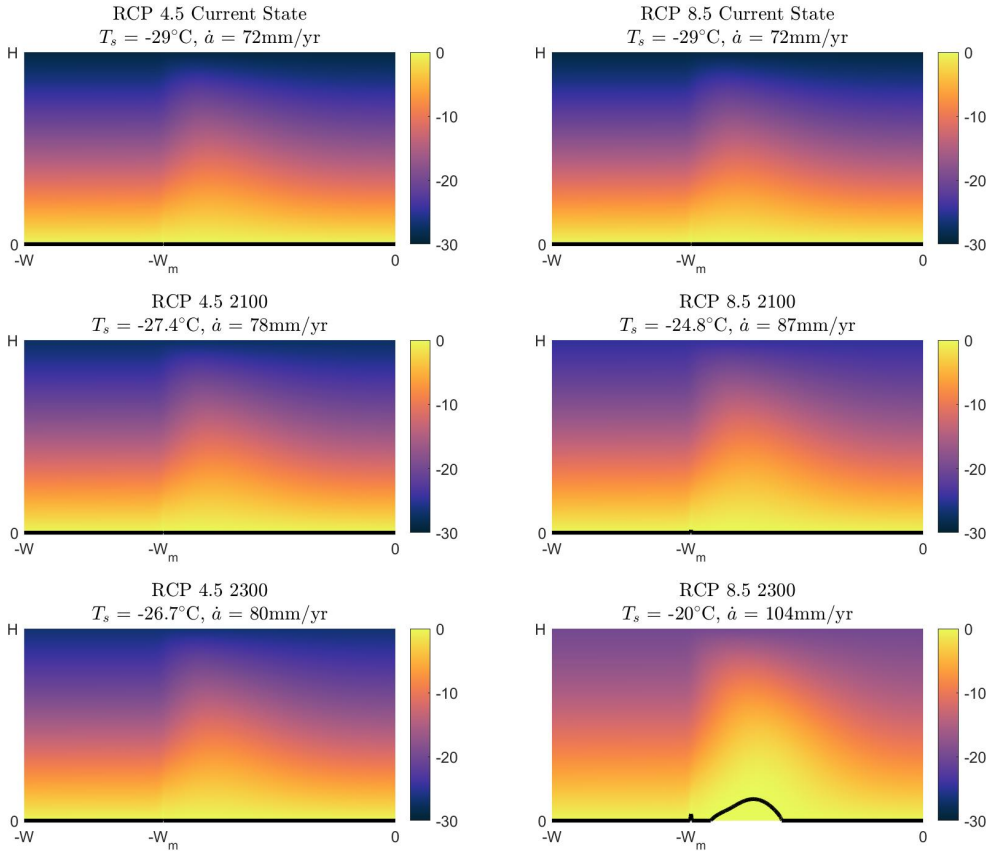

Figure C3: Modeled temperature profiles for the Bindschadler cross-section labeled "Right-Lower" on Fig. 4 from the main text under various climate forcings. The top row is under present day conditions, the middle row uses predicted conditions at year 2100 under emissions scenairos RCP 4.5 (left) and RCP 8.5 (right), and the bottom row are the same emissions scenarios forecast to 2300. The black solid line corresponds to the 0°C contour.

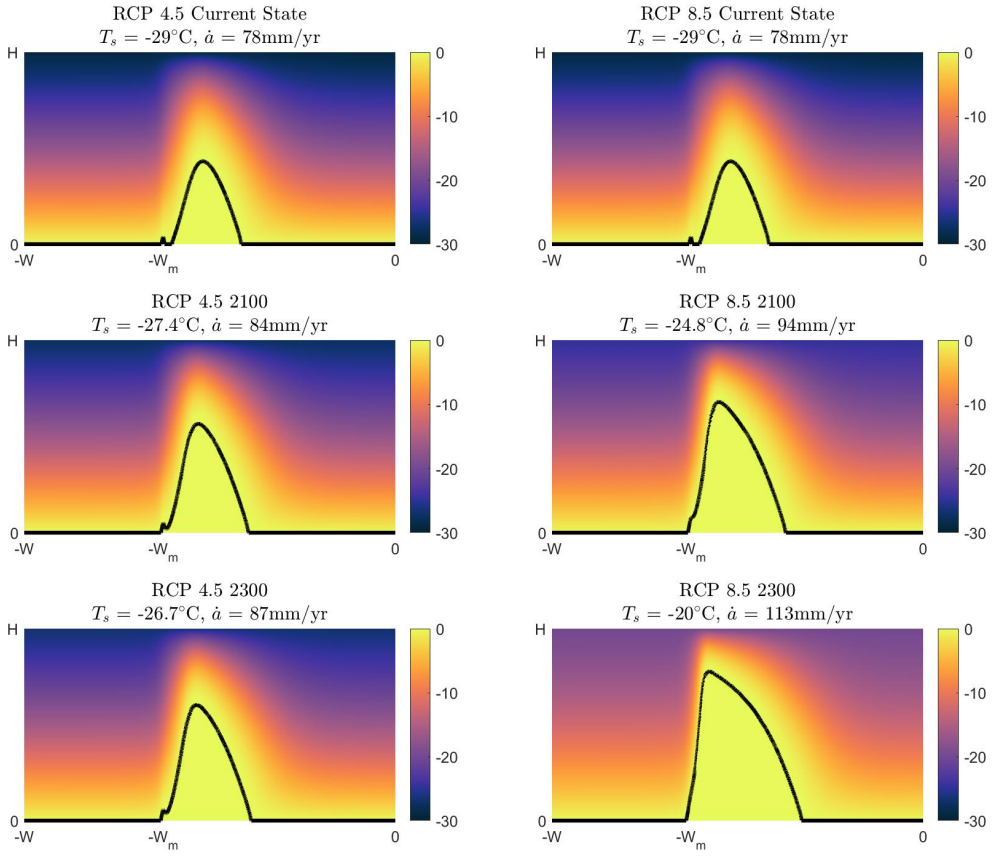

D HIGH RESOLUTION ANTARCTIC DATA

Here we provide high resolution images for each of the panels in Fig. 3 of the main text.

Figure D1: Antarctic surface velocity data from MEaSUREs [Rignot et al., 2011; Mouginot et al., 2012] and compiled in the QGIS package Quantarctica3 [Matsuoka et al., 2018]. The numbers correspond to the locations of the numbered ice streams in Table 3 from the main text.

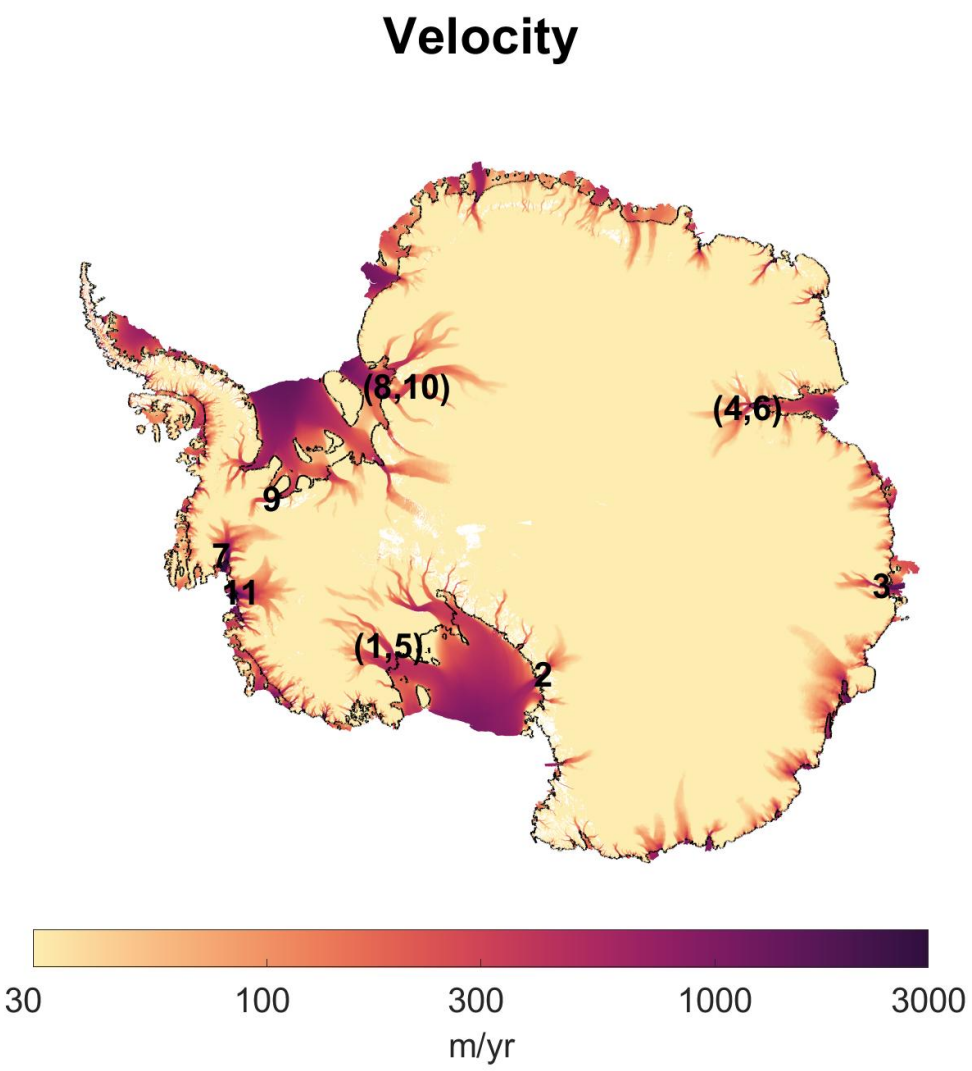

Figure D2: Antarctic surface mass balance data from RACMO 2.3 [Van Wessem et al., 2014] and compiled in the QGIS package Quantarctica3 [Matsuoka et al., 2018].

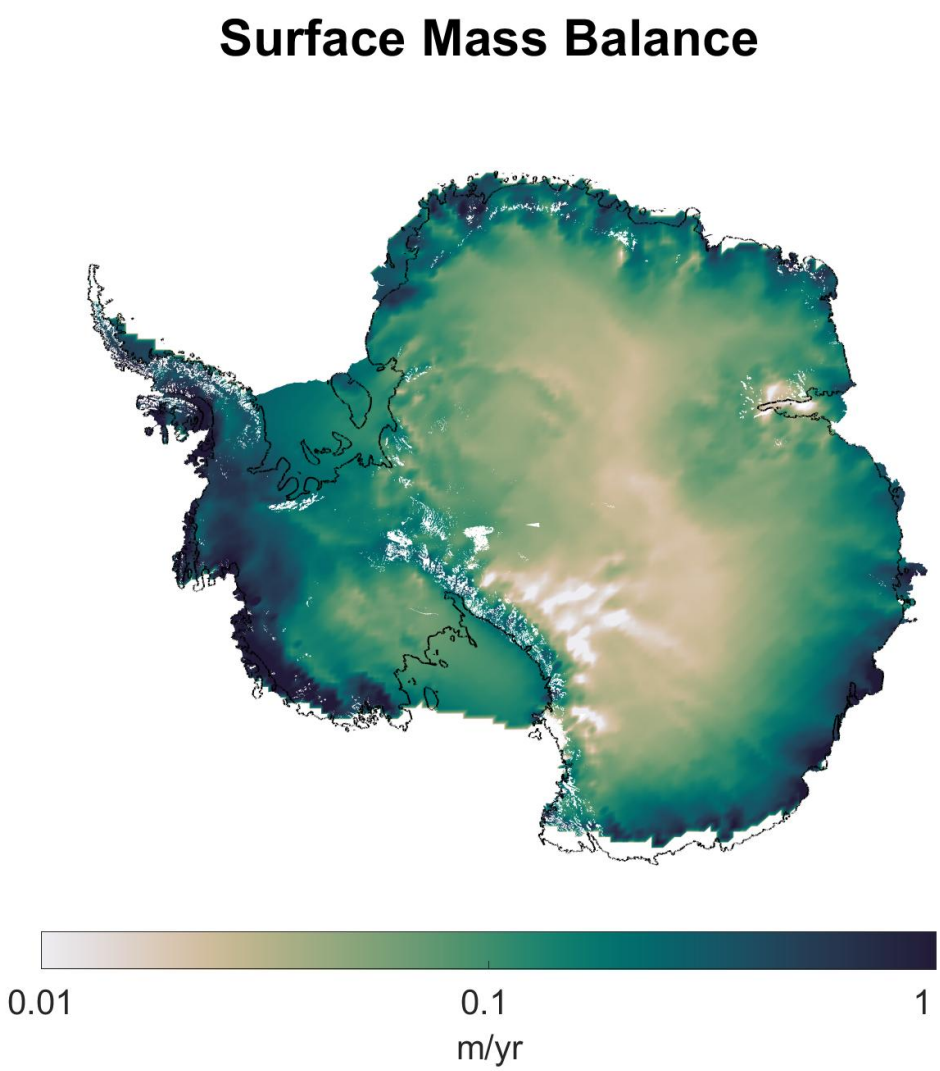

Figure D3: Antarctic ice thickness data from BEDMAP2 [Fretwell et al., 2013] and compiled in the QGIS package Quantarctica3 [Matsuoka et al., 2018].

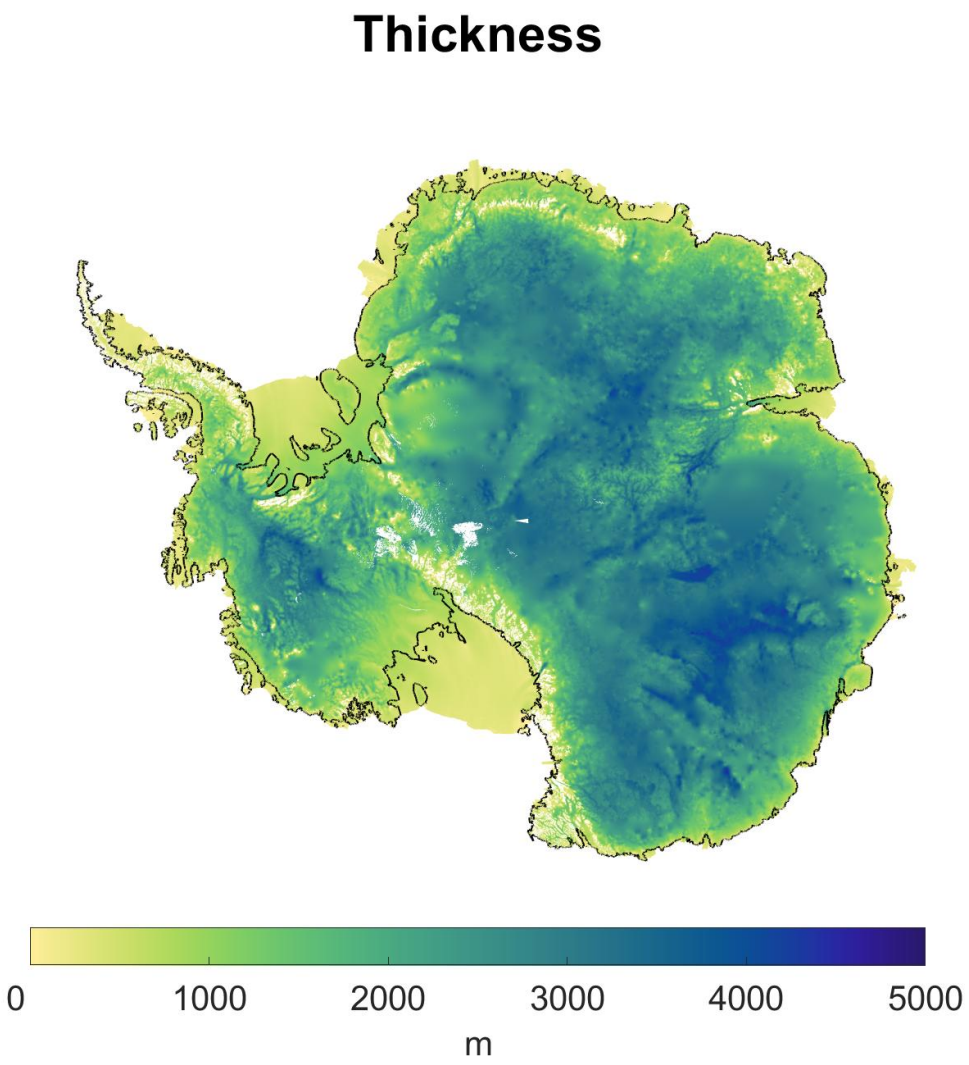

Figure D4: Antarctic surface temperature data from RACMO 2.3 [Van Wessem et al., 2014] and compiled in the QGIS package Quantarctica3 [Matsuoka et al., 2018].

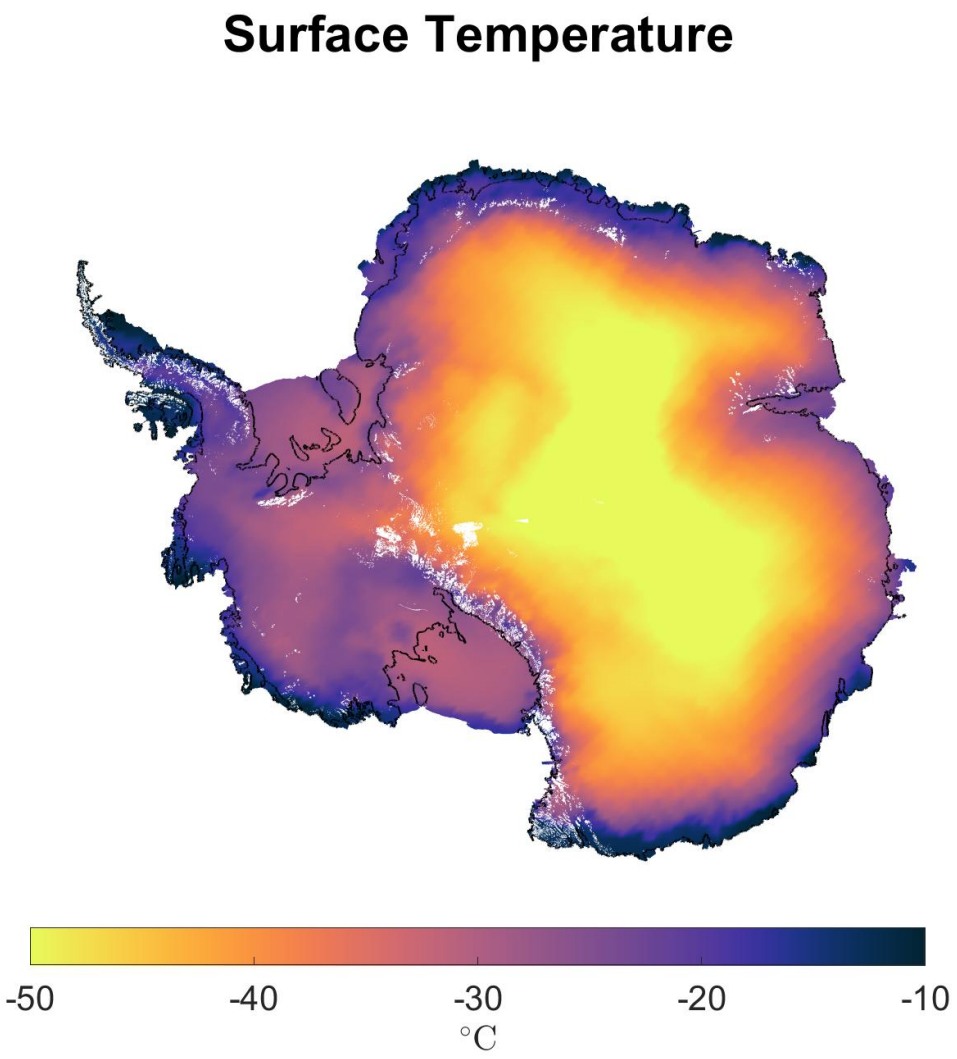

REFERENCES CITED

Bulthuis, K., Arnst, M., Sun, S., and Pattyn, F. (2019). Uncertainty quantification of the multi-centennial response of the antarctic ice sheet to climate change. *Cryosphere*, 13(4):1349–1380.

Carroll, D., Sutherland, D. A., Shroyer, E. L., Nash, J. D., Catania, G. A., and Stearns, L. A. (2015). Modeling turbulent subglacial meltwater plumes: Implications for fjord-scale buoyancy-driven circulation. *Journal of Physical Oceanography*, 45(8):2169–2185.

Cuffey, K. M. and Paterson, W. B. (2010). *The Physics of Glaciers Fourth Edition*.

Fretwell, P., Pritchard, H. D., Vaughan, D. G., Bamber, J. L., Barrand, N. E., Bell, R., Bianchi, C., Bingham, R. G., Blankenship, D. D., Casassa, G., Catania, G., Callens, D., Conway, H., Cook, A. J., Corr, H. F., Damaske, D., Damm, V., Ferraccioli, F., Forsberg, R., Fujita, S., Gim, Y., Gogineni, P., Griggs, J. A., Hindmarsh, R. C., Holmlund, P., Holt, J. W., Jacobel, R. W., Jenkins, A., Jokat, W., Jordan, T., King, E. C., Kohler, J., Krabill, W., Riger-Kusk, M., Langley, K. A., Leitchenkov, G., Leuschen, C., Luyendyk, B. P., Matsuoka, K., Mouginot, J., Nitsche, F. O., Nogi, Y., Nost, O. A., Popov, S. V., Rignot, E., Rippin, D. M., Rivera, A., Roberts, J., Ross, N., Siegert, M. J., Smith, A. M., Steinhage, D., Studinger, M., Sun, B., Tinto, B. K., Welch, B. C., Wilson, D., Young, D. A., Xiangbin, C., and Zirizzotti, A. (2013). Bedmap2: Improved ice bed, surface and thickness datasets for Antarctica. *Cryosphere*, 7(1):375–393.

Goldberg, D., Holland, D. M., and Schoof, C. (2009). Grounding line movement and ice shelf buttressing in marine ice sheets. *Journal of Geophysical Research: Earth Surface*, 114(4):1–23.

Golledge, N. R., Kowalewski, D. E., Naish, T. R., Levy, R. H., Fogwill, C. J., and Gasson, E. G. (2015). The multi-millennial Antarctic commitment to future sea-level rise. *Nature*, 526(7573):421–425.

Haseloff, M., Hewitt, I. J., and Katz, R. F. (2019). Englacial Pore Water Localizes Shear in Temperate Ice Stream Margins. *Journal of Geophysical Research: Earth Surface*, 124(11):2521–2541.

Haseloff, M., Schoof, C., and Gagliardini, O. (2015). A boundary layer model for ice stream margins. *Journal of Fluid Mechanics*, 781:353–387.

Haseloff, M., Schoof, C., and Gagliardini, O. (2018). The role of subtemperate slip in thermally driven ice stream margin migration. *Cryosphere*, 12(8):2545–2568.

Jacobson, H. P. and Raymond, C. E. (1998). Thermal effects on the location of ice stream margins. *Journal of Geophysical Research*, 103(B6):12111–12122.

Jenkins, A. (2011). Convection-driven melting near the grounding lines of ice shelves and tidewater glaciers. *Journal of Physical Oceanography*, 41(12):2279–2294.

Matsuoka, K., Skoglund, A., and Roth, G. (2018). Quantarctica.

Meyer, C. R. and Minchew, B. M. (2018). Temperate ice in the shear margins of the Antarctic Ice Sheet: Controlling processes and preliminary locations. *Earth and Planetary Science Letters*, 498:17–26.

Meyer, C. R., Yehya, A., Minchew, B., and Rice, J. R. (2018). A Model for the Downstream Evolution of Temperate Ice and Subglacial Hydrology Along Ice Stream Shear Margins. *Journal of Geophysical Research: Earth Surface*, 123(8):1682–1698.

Mouginot, J., Scheuch, B., and Rignot, E. (2012). Mapping of ice motion in antarctica using synthetic-aperture radar data. *Remote Sensing*, 4(9):2753–2767.

Pegler, S. S. (2018). Suppression of marine ice sheet instability. *Journal of Fluid Mechanics*, 857:648–680.

Perol, T. and Rice, J. R. (2015). Shear heating and weakening of the margins of West Antarctic ice streams. *Geophysical Research Letters*, 42:3406–3413.

Perol, T., Rice, J. R., Platt, J. D., and Suckale, J. (2015). Subglacial hydrology and ice stream margin locations. *Journal of Geophysical Research: Earth Surface*, pages 1352–1368.

Ranganathan, M., Minchew, B., Meyer, C. R., and Gudmundsson, G. H. (2020). A new approach to inferring basal drag and ice rheology in ice streams , with applications to West Antarctic ice streams. *EarthArXiv*.

Rignot, E., Mouginot, J., and Scheuchl, B. (2011). Ice flow of the antarctic ice sheet. *Science*, 333(6048):1427–1430.

Schoof, C. (2007). Ice sheet grounding line dynamics: Steady states, stability, and hysteresis. *Journal of Geophysical Research: Earth Surface*, 112(3):1–19.

Schoof, C. (2010). Ice-sheet acceleration driven by melt supply variability. *Nature*, 468(7325):803–806.

Schoof, C. (2012). Thermally driven migration of ice-stream shear margins. *Journal of Fluid Mechanics*, 712:552–578.

Suckale, J., Platt, J. D., Perol, T., and Rice, J. R. (2014). Deformation-induced melting in the margins of the West Antarctic ice streams. *Journal of Geophysical Research: Earth Surface*, 119(5):1004–1025.

Sutherland, D. A., Jackson, R. H., Kienholz, C., Amundson, J. M., Dryer, W. P., Duncan, D., Eidam, E. F., Motyka, R. J., and Nash, J. D. (2019). Direct observations of submarine melt and subsurface geometry at a tidewater glacier. *Science*, 365(6451):369–374.

Van Wessem, J. M., Reijmer, C. H., Morlighem, M., Mouginot, J., Rignot, E., Medley, B., Joughin, I., Wouters, B., Depoorter, M. A., Bamber, J. L., Lenaerts, J. T., Van De Berg, W. J., Van Den Broeke, M. R., and Van Meijgaard, E. (2014). Improved representation of East Antarctic surface mass balance in a regional atmospheric climate model. *Journal of Glaciology*, 60(222):761–770.

Weertman, J. (1974). Stability of the Junction of an Ice Sheet and an Ice Shelf. *Journal of Glaciology*, 13(67):3–11.